Materials & Design 257 (2025) 114531

Contents lists available at ScienceDirect

Materials & Design

journal homepage: www.elsevier.com/locate/matdes

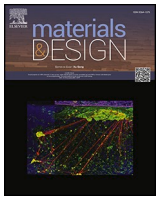

Revealing the mechanism of crystal orientation-dependent surface morphology and topography evolution in single-crystal ZnO using nanoindentation☆

Weihai Huang, Jiwang Yan *

Department of Mechanical Engineering, Faculty of Science and Technology, Keio University, 3-14-1 Hiyoshi, Kohoku-ku, Yokohama 223-8522, Japan

ARTICLE INFO

Keywords:
Single-crystal zinc oxide
Crystal anisotropy
Surface formation
Dislocation behavior
Nanoindentation

ABSTRACT

Single-crystal zinc oxide (ZnO) is an important optoelectronic material, but its micro/nanoscale mechanical behavior is poorly understood. In this study, nanoindentation tests were performed on various crystalline planes of ZnO crystals using a Berkovich indenter at different indenter orientations. The surface and subsurface characteristics of the different crystal planes were analyzed and compared. It was found that indentation on the (0001) plane activated both basal and pyramidal slip systems, which suppressed pile-up. Dislocation pinning caused pop-in events during loading and promoted edge crack formation during unloading due to high elastic recovery. Indentation on the (1−100) and (11−20) planes activated basal and prismatic slip systems. As these systems cannot accommodate dislocation glide along the [0001] direction, corner cracks easily initiated. Meanwhile, dislocations glided toward the surface with minimal resistance, thereby facilitating outward material flow and pile-up formation along the [11−20] and [1−100] directions. Indenter orientation variation did not alter slip system activation for any plane and had minimal impact on plastic flow trends. No phase transformation was detected on the indented surfaces, while dislocation-induced luminescence quenching was observed. This study reveals how crystal orientation governs surface evolution in ZnO, offering guidance for machining method development and processing parameter optimization.

1. Introduction

Single-crystal zinc oxide (ZnO) is a wide-bandgap semiconductor material categorized as a third-generation semiconductor. It exhibits a large exciton binding energy, high thermal conductivity, and chemical stability; thus, ZnO is highly suitable for applications such as blue/UV optoelectronics, transparent electronic circuits, and radiation-hardened electronics for space environments [1]. ZnO bulk crystals have a hexagonal wurtzite-type structure. Based on crystal growth orientation, ZnO wafers, oriented along three crystal planes, are typically available: the {0001} plane (*c*-plane), the {11−20} plane (*a*-plane), and the {1−100} plane (*m*-plane). As a single crystal, ZnO demonstrates unique mechanical properties depending on the crystal plane. For instance, the hardness of the *c*-plane is twice that of the *a*-plane, with values of 4.8 GPa and 2 GPa, respectively. It also demonstrates a hardness less than one-fourth that of gallium nitride, GaN, (20 GPa for the *c*-plane), which shares the same crystal structure as ZnO [2]. Furthermore, the measured mechanical properties of ZnO are highly sensitive to processing conditions, as surfaces polished on the same crystal plane with abrasives of different grit sizes may exhibit variations in hardness [3]. To improve the surface quality of ZnO, surface topographical features and surface layer properties are key factors to consider in machining processes.

Nanoindentation is a widely used technique for evaluating the mechanical properties of materials, including hardness [4], elastic modulus [5], and fracture toughness [6]. Compared to uniaxial testing, it is a relatively simple and nondestructive method for obtaining these properties at the micro- and nanoscale [7]. By analyzing precisely recorded nanoindentation load–displacement curves and the resulting surface and subsurface damage, this technique also helps in understanding the formation of defects in materials subjected to mechanical contact [8]. Several studies on the nanoindentation of ZnO have been conducted. Kucheyev et al. [9] found that slip is the primary mode of plastic deformation in *c*-plane ZnO, and it is related to the occurrence of pop-in events in nanoindentation, which are sudden bursts of indenter

☆ This article is part of a special issue entitled: 'Nanomechanical Testing 2024' published in Materials & Design.

* Corresponding author.
E-mail address: yan@mech.keio.ac.jp (J. Yan).

https://doi.org/10.1016/j.matdes.2025.114531
Received 29 May 2025; Received in revised form 23 July 2025; Accepted 5 August 2025
Available online 6 August 2025

displacement appearing as plateaus in load–displacement curves. Using pop-in events as indicators, the elastic–plastic threshold was found to increase with the loading rate. Subsequently, a transmission electron microscope (TEM) was applied to further reveal that the propagation of slip along the pyramidal and basal planes causes severe subsurface damage, extending deep into the bulk of the material and laterally well beyond the residual indent [10]. Similarly, Zhu et al. [11] reported that in nanoindentation tests on *a*-plane ZnO using a Berkovich indenter, higher strain rates led to an increase in both the critical load and the width of the pop-in events, indicating a strain-rate-dependent elastic–-plastic transition behavior. Kim et al. [12] evaluated the creep behavior of *c*-plane ZnO under both elastic and elastic–plastic deformation regimes by applying different maximum loads. The creep deformation was more pronounced in the elastic–plastic regime. Gao et al. [13] characterized the load-dependent mechanical properties of *c*-plane ZnO through nanoindentation/scratching, and developed analytical stress-field models to predict crack initiation and propagation in these processes. Basu et. al [14], through the analysis of slip bands on the surface, reported that during *c*-plane nanoindentation, glide occurs on both basal and pyramidal planes, whereas during *a*-plane nanoindentation, glide primarily occurs on basal planes. This finding explained why the hardening rates are higher for *c*-plane nanoindentation than for *a*-plane nanoindentation. Sung et al. [15] characterized nano- and micro-mechanical properties, including modulus, hardness, yield stress, and critical resolved shear stress of *c*-, *a*-, and *m*-plane ZnO via nanoindentation and micropillars compression tests. The trace of dislocation slip on each crystal plane of ZnO was also observed. Juday et al. [16] compared the distribution of surface structural defects induced by nanoindentation on *c*-, *a*-, and *m*-plane ZnO. The compressive strain and tensile strain on each plane were visualized via cathodoluminescence (CL) spectroscopy. Lin et al. [17] investigated the creep behavior of *c*-, *a*-, and *m*-plane ZnO in nanoindentation experiments. The stress exponent was found to vary under different conditions, implying that the diffusion and dislocation mechanisms may operate differently depending on the planes and applied loads. In recent, Li et al. [18] prepared an nanoindentation sample with a surface oriented 45° off the (0001) plane to preferentially activate basal slip on the (0001) plane. They found that, under light illumination, both dislocation motion and creep deformation could be suppressed. In addition to testing the 45° off-(0001) plane, Oguri et al. [19] further conducted creep experiments on the *c*-, *a*-, and *m*-planes of ZnO under controlled light illumination. Their results confirmed that light suppresses indentation-induced creep deformation on all surface orientations, although the degree of suppression varies depending on the crystal plane.

The machining community is increasingly using nanoindentation to investigate phenomena at the microscopic scale during the material removal process, as the compressive stress generated during nanoindentation resembles that produced in front of the cutting tool during machining [20]. The morphology and topography of the indented surface are among the most valuable aspects, as they directly reflects material flow and fracture during mechanical loading [21], offering essential insights into side flow-related chip and surface formation [22,23], and crack initiation [24,25] in mechanical processing. Moreover, these surface features can be influenced by both material crystal orientation [26] and indenter geometry [27]. This information is valuable for determining optimal processing directions in ultraprecision machining [28]. Characterization of the difference between the maximum and residual depths of indentation on various crystal planes suggests that the grain boundary steps formed on the machined surface of polycrystalline materials may be caused by differences in elastic recovery induced by crystal orientation [29]. Fig. 1 provides an overview of the relation between nanoindentation and machining processes. However, previous studies on nanoindentation of ZnO, primarily conducted by the materials science and solid-state physics communities, have focused on investigating the defects formation in ZnO bulks by analyzing load–displacement curves. Some studies have further employed CL and TEM characterization. Little attention has been given to the surface morphology and topography of residual indents, nor have they compared these surface features across different ZnO crystal planes. The influence of indenter geometry on the surface formation during nanoindentation on various ZnO crystal planes has also not been reported. In summary, the interrelationship among the surface morphology and topography of residual indents, the indenter geometry, and the nanoindentation-induced surface and subsurface defects in ZnO crystals remains unclear. Additionally, the mechanism of surface morphology and topography evolution dependent on crystal orientation has not yet been investigated. These knowledge gaps have constrained the development of machining methods for ZnO crystals, which are currently fabricated primarily through polishing.

In this study, nanoindentation tests were conducted on *c*-plane (0001), *m*-plane (1−100), and *a*-plane (11−20) ZnO crystals using a Berkovich indenter. For each crystal plane, two indenter orientation angles, with an interval of 30°, were employed. The surface morphology and topography of the residual indents were characterized using scanning electron microscopy (SEM) and atomic force microscopy (AFM). The nanoindentation-induced surface and subsurface defects were

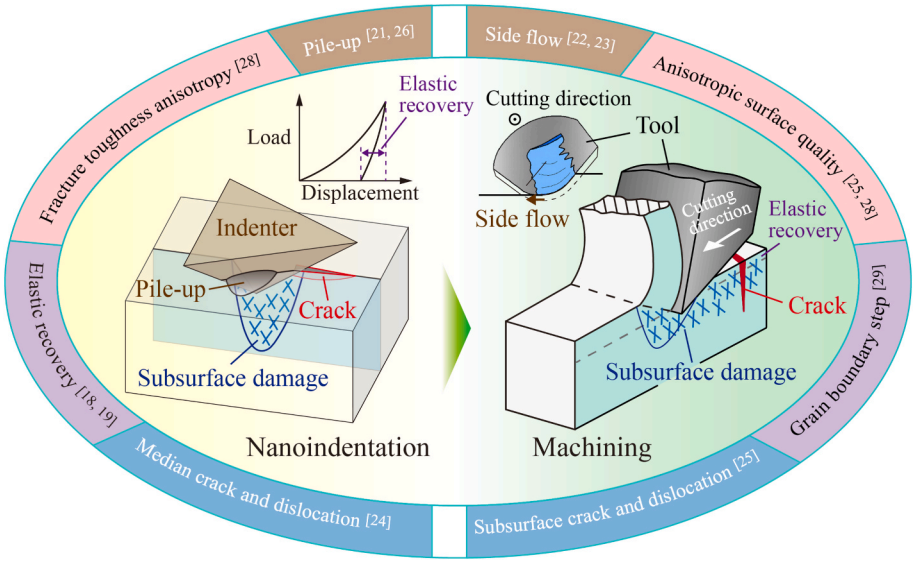

Fig. 1. What nanoindentation tests can reveal about machining processes.

subsequently examined by cathodoluminescence (CL), Raman microspectrometry, and cross-sectional transmission electron microscopy (XTEM). The mechanism underlying the crystal orientation-dependent evolution of surface morphology and topography was investigated by correlating macroscopic material deformation with microstructural defect formation and by analyzing the load–displacement (*P-h*) curves. This study could help to advance the understanding of the surface formation mechanisms of ZnO crystals under machining processes. The findings are expected to provide valuable insights for developing and optimizing ultra-precision and nanometric machining processes for ZnO substrates with high surface integrity.

2. Experimental procedure

Single-crystal ZnO has hexagonal (Wurtzite) structure, as illustrated in Fig. 2(a). Three ZnO wafers, each measuring 5 × 5 × 0.5 mm and oriented along *c*-plane (0001), *m*-plane (1−100), and *a*-plane (11−20), were used as workpieces. The surfaces of the workpieces were smoothed through chemo-mechanical polishing. The surface roughness values for the *c*-plane, *m*-plane, and *a*-plane workpieces were 1.1 nm, 1.3 nm, and 1.0 nm Sa, respectively, measured over areas of 350 μm^2.

Nanoindentation tests were performed using a nanoindentation device (Nano Indenter G200, KLA Corp., USA). A Berkovich diamond tip was employed, with a tip radius of approximately 260 nm, as measured from the profile of one of the indenter's facets (Fig. S1). The indentation process is schematically illustrated in Fig. 2(b). To investigate the effects of crystal orientation and tool geometry on deformation behavior, indentation tests were performed on each crystal plane at two indenter orientation angles, with an interval of 30°, as illustrated in Fig. 2(c). For clarity, the indenter orientation was labeled as the 0-degree indentation (represented by the red solid line) and the 30-degree indentation (represented by the navy-blue dashed line). In this way, depending on the indenter orientation (i.e., 0-degree or 30-degree indentations), for *c*-plane nanoindentation, three ridges of the indenter were aligned parallel to the <11−20> and <1−100> directions, respectively. For *m*-plane nanoindentation, one ridge was aligned parallel to the [0001] and [11−20] directions, respectively; for *a*-plane nanoindentation, one ridge was aligned parallel to the [0001] and [1−100] directions, respectively.

An allowable drift rate of 0.5 nm/s was set. In this case, the indenter began approaching the workpiece surface only after the measured drift rate had fallen below this threshold. During the nanoindentation, the applied load (*P*) increased from 0 to a maximum value (P_{max}) in the loading phase. The load was held at P_{max} for 1 s, after which it was reduced to 0 in the unloading phase. For each indentation, the loading and unloading rates were 1 mN/s to eliminate variations in the elastic–plastic threshold caused by changes in the loading rate [9]. Three P_{max} values, including 20, 50, and 200 mN, were applied. The indentation parameters are summarized in Table 1. Since the hardness of ZnO is low, the maximum applied load was relatively small, and the primary focus of this study was on indentation-induced surface and subsurface morphology rather than material property characterization, frame stiffness correction was not considered. A 3 × 3 square array of indentations was employed in each group of indentation tests. The pitch of the indentations ranged from 30 to 80 μm, depending on the maximum loads and the crystal planes.

After the nanoindentation, the surface morphologies and structural defects of the residual indents were examined using a scanning electron microscope (SEM) equipped with a cathodoluminescence (CL) detector. The CL detector employs a photomultiplier tube with a sensitivity range from 300 nm to 650 nm with a peak around 420 nm. The surface topographies of the residual indents were measured using an atomic force microscope (AFM). Additionally, the surface structural characteristics of the residual indents were analyzed using a micro-laser Raman microscope. Finally, a cross-sectional transmission electron microscope (XTEM) was employed to examine the subsurface structural characteristics of the residual indents formed under a P_{max} of 20 mN. Focused ion

Table 1
Parameters applied to nanoindentation on ZnO crystals.

Parameters	values
Maximum load (P_{max})	20, 50, 200 mN
Loading/unloading rate	1 mN/s
Holding time at P_{max}	1 s
Indenter geometry	Berkovich
Indenter orientation	0°, 30°

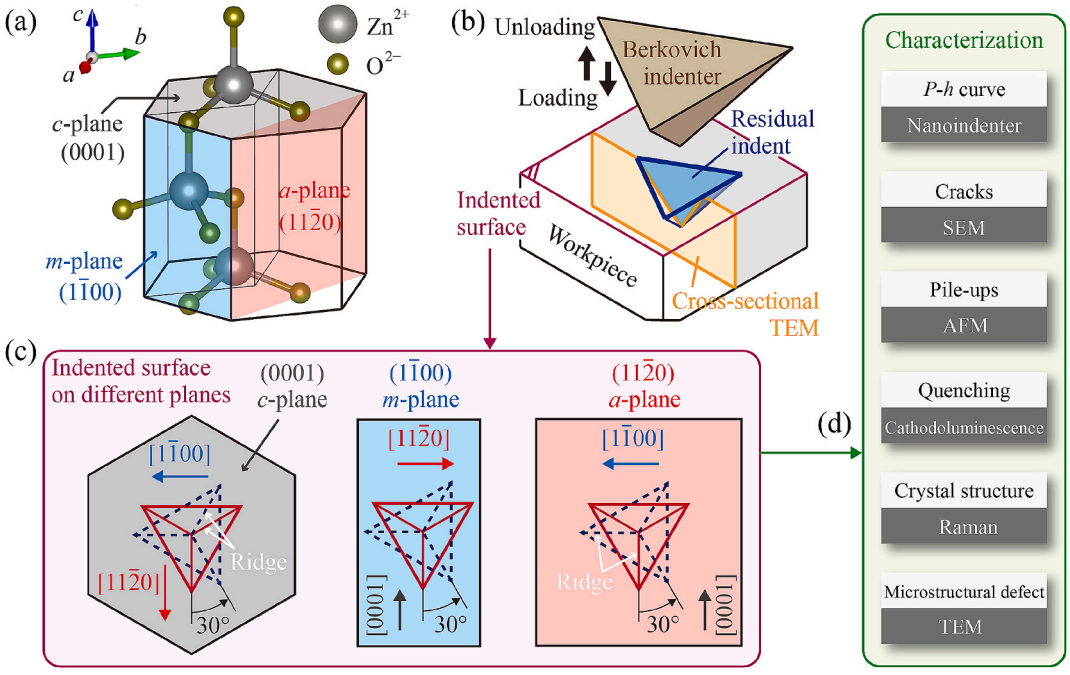

Fig. 2. Nanoindentation experiment setup: (a) schematic of the crystal structure of the ZnO workpiece; (b) schematic of the indentation process; (c) schematic of indentations on three crystal planes, with two indenter orientations applied on each plane; (d) surface/subsurface characterization, including feature-method pairs.

beam (FIB) milling was used to prepare the XTEM samples.

3. Results

3.1. Load-displacement curve characteristics

Fig. 3(a) shows the load–displacement curves of 0-degree and 30-degree indentations on the (0001) plane of ZnO at various P_{max}. Under both indenter orientations, the displacement gradually increased as the load increased from zero but showed a sudden discontinuity, known as a pop-in event, when the load reached approximately 15 mN. More pop-in events randomly occurred as the load increased further, as shown in the curves for P_{max} values of 50 mN and 200 mN. Nevertheless, when the load reached P_{max}, the displacements of the indenters (i.e., the maximum indentation depth h_{max}) were similar for both orientations. Unlike the indentations on the (0001) plane, the load–displacement curves of 0-degree and 30-degree indentations on the (1−100) and (11−20) planes of ZnO exhibited no evidence of pop-in events, even at P_{max} of 200 mN, as plotted in Fig. 3(b,c). This phenomenon was highly repeated, as demonstrated in Fig. S2.

Fig. 4(a) shows a summary of h_{max} for various crystal planes under different loads. Under the same load, it was observed that the h_{max} on the (11−20) plane is slightly greater than that on the (1−100) plane, both of which are significantly greater than the h_{max} observed on the (0001) plane. This is consistent with the fact that *c*-plane ZnO is much harder than *m*-plane and *a*-plane ZnO. On the (1−100) and (11−20) planes, at the same P_{max}, the displacement produced by a 0°-oriented indenter was always greater than that produced by a 30°-oriented indenter. Fig. 4(b) compares the elastic recovery rate (ERR) under various conditions, defined as the ratio of the difference between the h_{max} and the residual indentation depth (h_{res}) to the h_{max}. In general, for each crystal plane, as the P_{max} increased, the ERR decreased. Under the same load, the (0001) plane demonstrated significantly stronger elastic recovery capacity than the (1−100) and (11−20) planes. For the (1−100) and (11−20) planes, the ERR for the 30-degree indentations was larger than that for the 0-degree indentations. The difference in ERR is expected to be significantly influenced by pile-up formation. The (0001) plane, which exhibited no pile-up formation, showed a much higher ERR compared to the (1−100) and (11−20) planes, where significant pile-up was observed. In contrast, microcracks appeared to have a smaller effect on ERR, as the 30°-oriented indentations with radial cracks on the (1−100) and (11−20) planes exhibited even higher ERRs than the 0°-oriented indentations without radial cracks. These behaviors will be thoroughly presented in the following sections.

3.2. Surface morphologies

Fig. 5 shows the morphologies of the residual indents on the (0001) plane. Wherein, Fig. 5(a-c) show the indents produced by a 0°-oriented indenter under various P_{max} values. At P_{max} = 20 mN, no cracks were observed on the indented surface. As the P_{max} increased to 50 mN, short cracks were initiated along the ridges and edges of the indent. When the P_{max} was further increased to 200 mN, ridge cracks and edge cracks within the indent extended, while no additional cracks were generated in the surrounding regions. Fig. 5(d-f) show the indents produced by a 30°-oriented indenter under various P_{max} values. In contrast to the 0-degree indentation, slight cracking occurred along both the ridges and edges of the indent at P_{max} = 20 mN. As P_{max} increased to 50 and 200 mN, the length of ridge and edge cracks increased accordingly within the indent. Generally, under the same P_{max}, the extent of cracking in 0-degree indentations was less than that in 30-degree indentations on the (0001) plane, both in terms of the number and length of cracks. This may be attributed to the fact that the edges of the 0-degree indentations are parallel to the {11−20} planes, while the edges of the 30-degree indentations are parallel to the {1−100} planes. In addition, the cleavage energy of the {11−20} planes is higher than that of the {1−100} planes [30]. However, it is worth noting that when performing indentation on the GaN (0001) plane, no cracks were observed on the indented surface, even when the P_{max} reached 200 mN [31]. Moreover, as shown in Fig. 5, the cracks that were initially generated at the ridges of the indents progressively deviated from these ridges as P_{max} increased, suggesting that ridge cracks likely formed during the loading phase. This occurred because the indenter's penetration direction was not perfectly normal to the workpiece surface, resulting in an offset between the indenter ridges at varying indentation depths when viewed perpendicular to the surface. In other words, during the loading phase, cracks were initiated in the material along the indenter ridges once a critical load was reached. As the load continued to increase, the indenter ridges deviated from the generated cracks while the cracks extended along the original path. Eventually, an offset formed between the cracks and the ridges of the indents. On the other hand, the cracks observed at the edges of the indents were considered to have been initiated during the unloading phase. This inference is supported by the fact that, regardless of the P_{max} values and the sizes of the indents, these cracks consistently propagated along the edges. In addition, none of the three facets of the indents exhibited cracks parallel to the edge cracks. Such edge cracks were also observed in the indentation of fused silica, which has high elastic recovery [32]. The cracks in Fig. 5 are enlarged and presented in Fig. S3. The residual indents exhibited high repeatability; an additional set of residual indents, induced under the same conditions as in Fig. 5, is provided in Fig. S4.

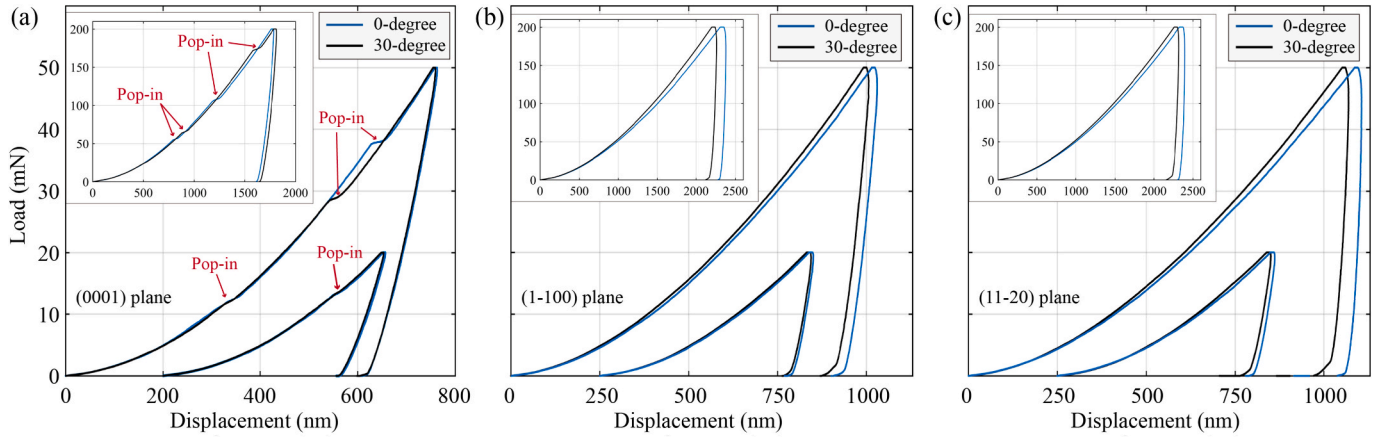

Fig. 3. Load-displacement curves of nanoindentation tests conducted with a maximum load (P_{max}) of 20, 50, and 200 mN on (a) the (0001) plane, (b) the (1−100) plane, and (c) the (11−20) plane in ZnO crystals. The curves at a P_{max} of 20 mN have been shifted along the displacement axis for improved clarity.

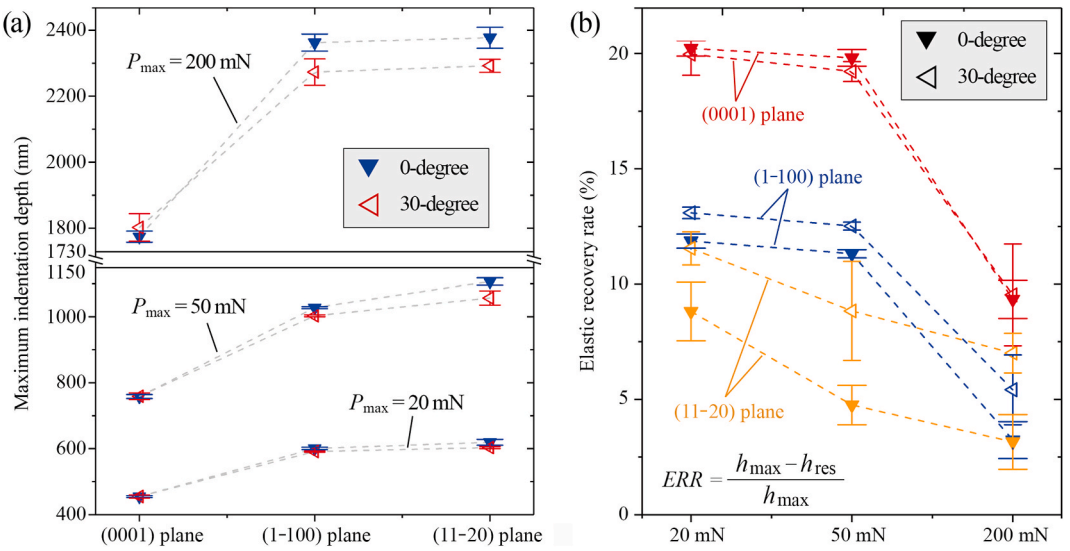

Fig. 4. Comparison of the indentation characteristics: (a) maximum indentation depth (h_{max}), and (b) elastic recovery rate (ERR), under various crystal planes and maximum loads (P_{max}).

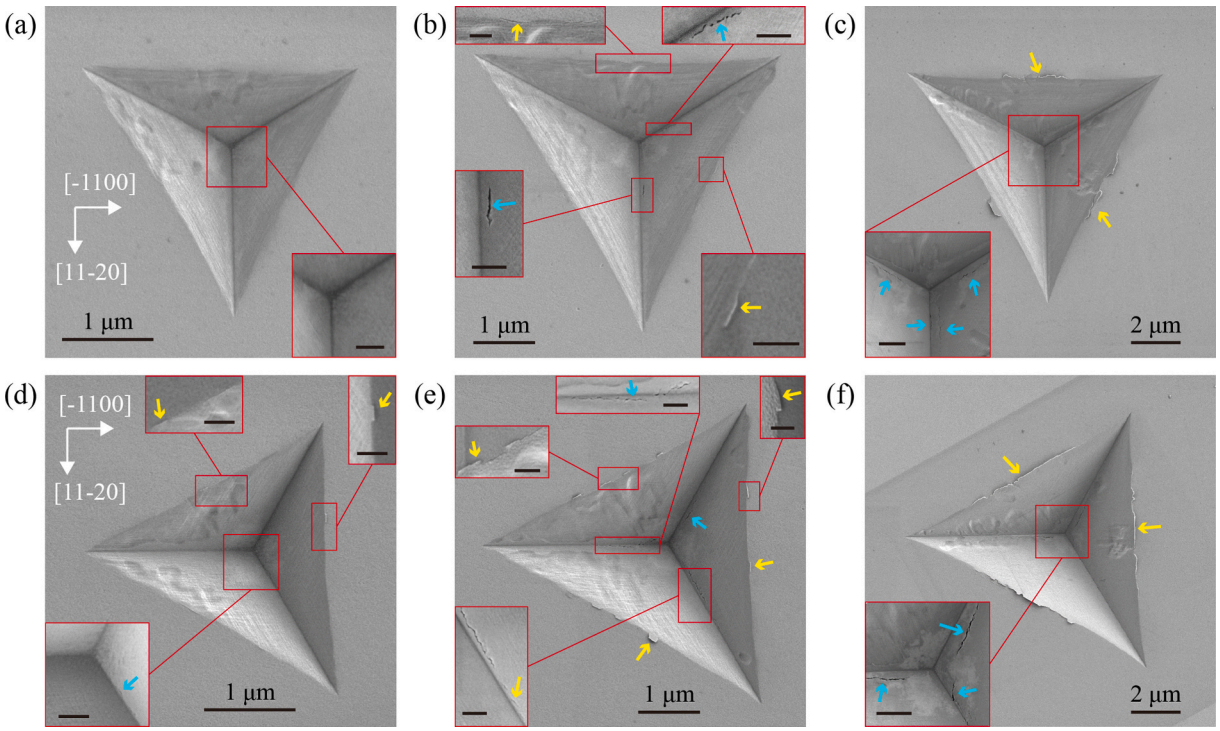

Fig. 5. SEM images showing the morphologies of residual indents on the (0001) plane of ZnO crystals: (a-c) 0-degree indentation at a maximum load (P_{max}) of 20, 50, and 200 mN; (d-f) 30-degree indentation at a P_{max} of 20, 50, 200 mN. The yellow and cyan arrows indicate the edge and ridge cracks, respectively. The scale bars in the insets of (a, b, d, and e) are 200 nm, and in (c, f) are 600 nm. (For interpretation of the references to colour in this figure legend, the reader is referred to the web version of this article.)

Fig. 6 shows the morphologies of the residual indents produced on the (1−100) plane under various conditions. Unlike those on the (0001) plane, the edges of the indents on the (1−100) plane became curved, regardless of the indenter orientation, as marked in Fig. 6(a,d), which is attributed to pile-up formation. For the 0-degree indentations, as shown in Fig. 6(a-c), pile-ups were formed on both the left and right sides of the indents (i.e., at the two symmetrical inclined edges). The path connecting these two pile-ups passed through the indentation center and was parallel to the [11−20] direction. Shear bands (SB), which were characterized by dense and curved lines, were formed on the surface of the pile-up areas as a result of significant plastic material flow [33]. No cracks formed in the indents produced at P_{max} values of 20 and 50 mN, while ridges cracks were observed at a P_{max} of 200 mN. For the 30-degree indentations, as shown in Fig. 6(d-f), pile-ups also formed on the left and right sides of the indents (i.e., at one corner and one vertical edge), accompanied by shear bands. The path connecting these two pile-ups remained parallel to the [11−20] direction. However, compared to the 0-degree indentation, additional slip traces, appearing as long, straight lines, were observed on the surface outside the indents, parallel to the [11−20] direction. These slip traces are believed to result from

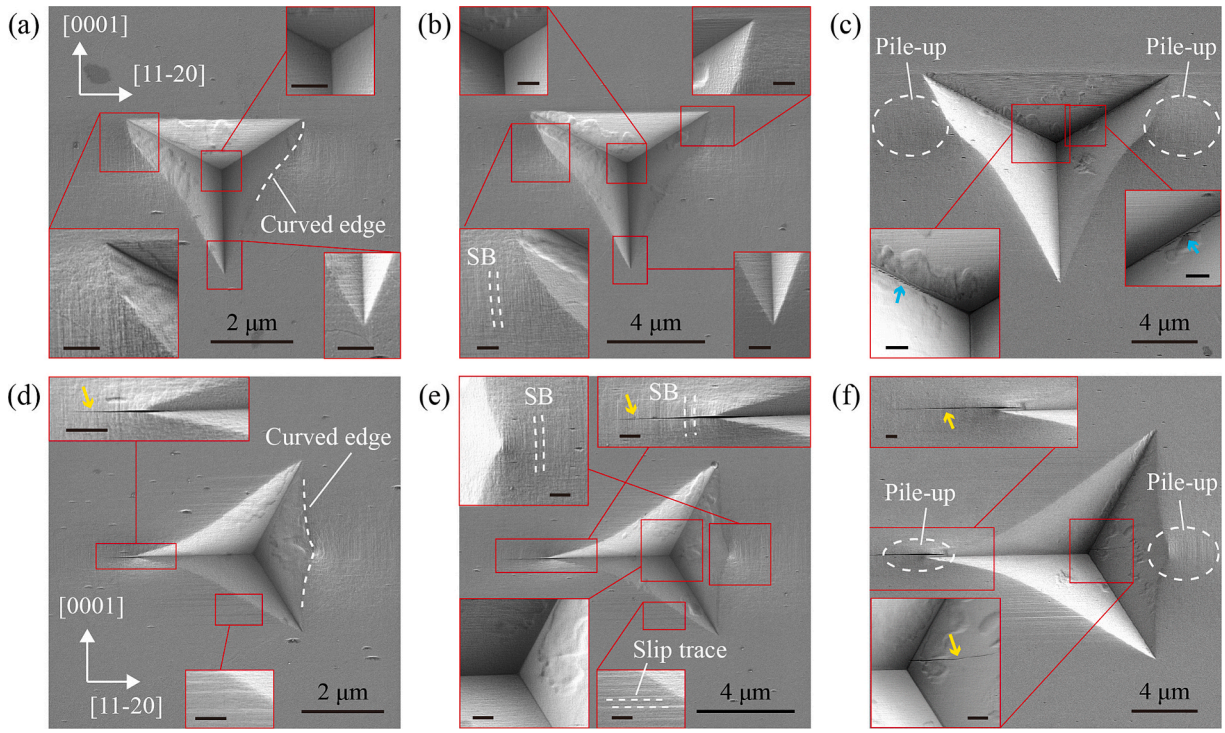

Fig. 6. SEM images showing the morphologies of residual indents on the (1−100) plane of ZnO crystals: (a-c) 0-degree indentation at a maximum load (P_{max}) of 20, 50, and 200 mN; (d-f) 30-degree indentation at a P_{max} of 20, 50, 200 mN. The yellow and cyan arrows mark the microcracks. SB refers to shear bands. The scale bars in the insets of (a, b, d, and e) are 200 nm, and in (c, f) are 600 nm. (For interpretation of the references to colour in this figure legend, the reader is referred to the web version of this article.)

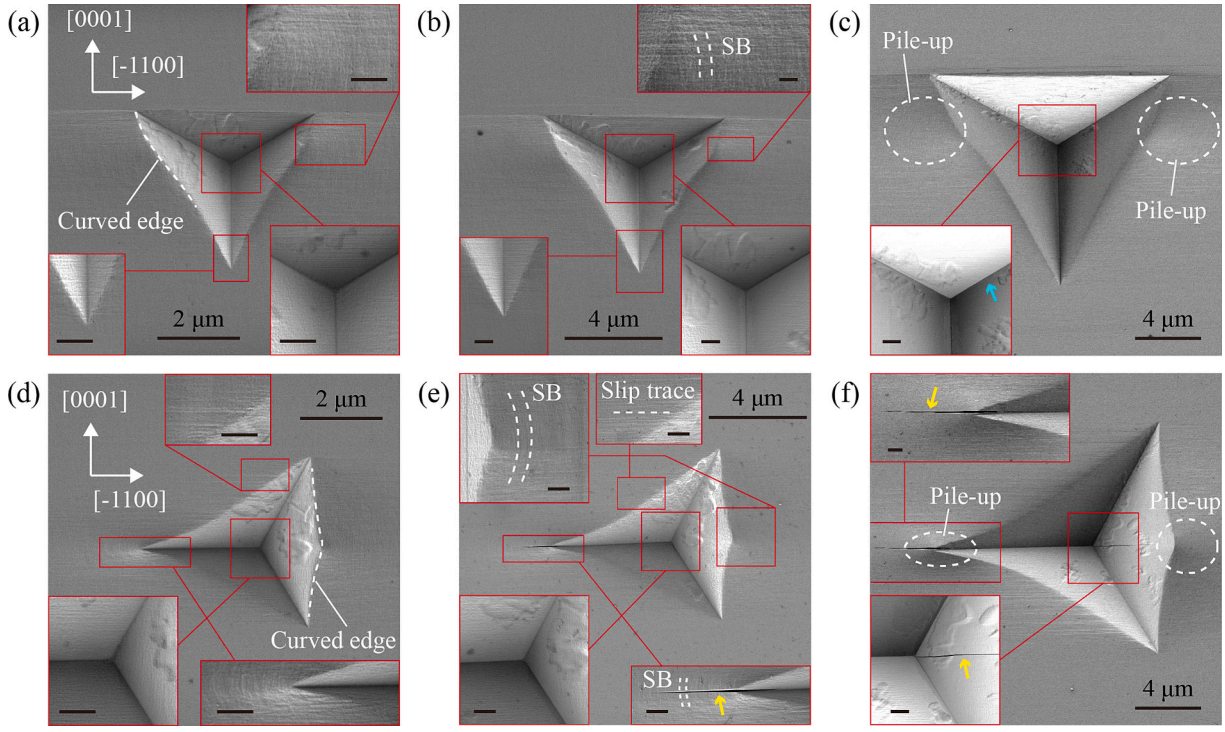

Fig. 7. SEM images showing the morphologies of residual indents on the (11−20) plane of ZnO crystals: (a-c) 0-degree indentation at a maximum load (P_{max}) of 20, 50, and 200 mN; (d-f) 30-degree indentation at a P_{max} of 20, 50, 200 mN. The yellow and cyan arrows mark the microcracks. SB refers to shear bands. The scale bars in the insets of (a, b, d, and e) are 200 nm, and in (c, f) are 600 nm. (For interpretation of the references to colour in this figure legend, the reader is referred to the web version of this article.)

intersections of activated slip planes inside the workpiece material with the workpiece surface [34]. Moreover, at P_{max} values of 20 and 50 mN, a long crack was initiated at one corner of each indent and propagated outward along the [11−20] direction. In crystalline materials, this corner crack, also known as a radial crack, is typically generated during the loading phase [35]. As P_{max} increased to 200 mN, an additional crack initiated at the center of the indent and propagated on one facet of the indent in the same direction as the corner crack. The above results indicate that, on the (1−100) plane, plastic flow of the material always occurs along the [11−20] direction, regardless of the indenter orientation. However, the indenter orientation significantly affects the critical load for the transition from plastic to brittle behavior. Specifically, the (1−100) plane exhibits better plasticity than the (0001) plane when a 0°-oriented indenter is used, while it exhibits more brittleness when a 30°-oriented indenter is used. This also implies that, during machining, the (1−100) plane-oriented wafers exhibit stronger fracture anisotropy than the (0001) plane-oriented wafers. The cracks and slip traces shown in Fig. 6 are enlarged and presented in Fig. S5. The residual indents exhibited high repeatability; an additional set of residual indents, induced under the same conditions as in Fig. 6, is provided in Fig. S6.

Fig. 7 presents the morphologies of the residual indents on the (11−20) plane produced under various conditions, whose surface features, including curved indent edges, shear bands, and slip traces, were similar to those observed on the (1−100) plane. The pile-up formation direction also remained independent of the indenter orientation. However, the directions of pile-up formation and slip traces shifted to the [1−100] direction. For the 0-degree indentations, as shown in Fig. 7(a-c), no cracks formed in the indents produced at P_{max} values of 20 and 50 mN, while slight cracks initiated along the ridges of the indents at P_{max} of 200 mN. For the 30-degree indentations, as shown in Fig. 7(d-f), no cracks were observed on the indented surface at P_{max} of 20 mN; however, at P_{max} of 50 mN, a corner crack initiated and propagated along the [1−100] direction. When P_{max} increased to 200 mN, an additional crack developed at the center of the indent and propagated in the same direction as the corner crack, within one facet of the indent. The above results suggest that, on the (11−20) plane, plastic flow of the material consistently occurs along the [1−100] direction, regardless of the indenter orientation. The (11−20) plane exhibits significant fracture anisotropy, similar to the (1−100) plane. However, under identical indentation conditions, the cracks formed on the (11−20) plane are less severe than those formed on the (1−100) plane. Enlarged views of the cracks in Fig. 7 are provided in Fig. S7. Fig. S8 shows another set of highly repeatable residual indents made under the same conditions as Fig. 7.

3.3. Surface topographies

To further investigate the deformation behavior of each crystal plane, three-dimensional surface topographies of the residual indents on these planes at P_{max} values of 20 and 50 mN were examined. Fig. 8(a,e) and Fig. 8(b,f) illustrate the topographies of the indented surfaces on the (0001) plane for the 0-degree and 30-degree indentations, respectively. Cross-sectional profiles of the indents for the 0-degree and 30-degree indentations were extracted along the <11−20> and <−1100> directions, respectively, which are aligned with the ridges of these indents. According to the cross-sectional profiles (Fig. 8(c,d,g,h)), it was observed that, regardless of the indenter orientation, neither pile-up nor sink-in formation occurred on the indented surfaces. It has been known that, during nanoindentation, materials with a high yield strength-to-Young's modulus ratio (Y/E) consistently exhibit sink-in, regardless of the strain hardening exponent [36]. In contrast, for materials with a low Y/E ratio, the occurrence of pile-up or sink-in depends on their strain hardening behavior: pile-up tends to occur in materials with low strain hardening, while sink-in is typically observed in those with high strain hardening [37,38]. Therefore, it can be inferred that ZnO exhibits a relatively low Y/E ratio. During nanoindentation of the (0001) plane, the plastic deformation of ZnO is neither highly localized around the indentation area nor characterized by rapid strain hardening near the indenter.

The topographies of the indented surfaces on the (1−100) plane for the 0-degree and 30-degree indentations are illustrated in Fig. 9(a, e) and Fig. 9(b, f), respectively. These results confirm the observation in Fig. 6 that pile-ups formed along the [11−20] direction, regardless of the indenter orientation. Subsequently, for both 0-degree and 30-degree indentations, a cross-sectional profile (A-A') of the indent was extracted along the [11−20] direction through the highest point of the pile-ups at

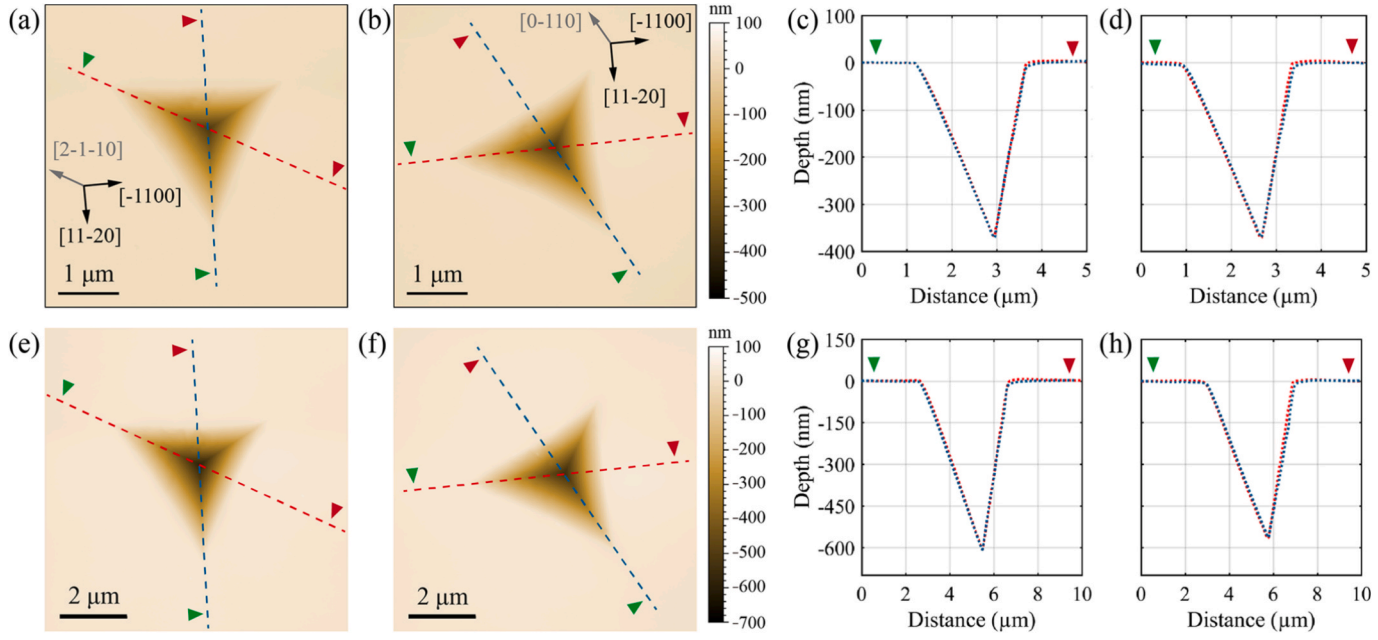

Fig. 8. Topographies of residual indents on the (0001) plane of ZnO crystals: (a, b) AFM images, and (c, d) cross-sectional profiles of the 0-degree and 30-degree indentations at a maximum load (P_{max}) of 20 mN. Similarly, (e, f) are AFM images, and (g, h) are cross-sectional profiles of the 0-degree and 30-degree indentations at a P_{max} of 50 mN.

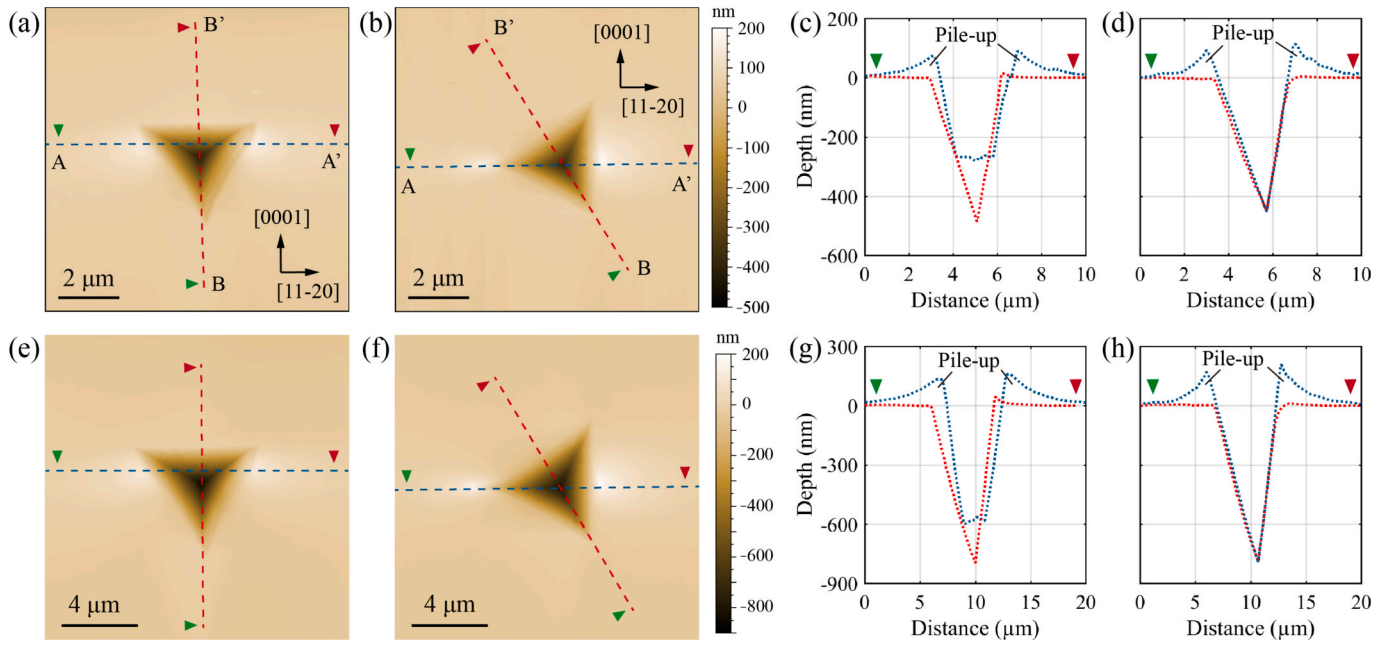

Fig. 9. Topographies of residual indents on the (1−100) plane of ZnO crystals: (a, b) AFM images, and (c, d) cross-sectional profiles of the 0-degree and 30-degree indentations at a maximum load (P_{max}) of 20 mN. Similarly, (e, f) are AFM images, and (g, h) are cross-sectional profiles of the 0-degree and 30-degree indentations at a P_{max} of 50 mN.

the two sides of the indents. Another cross-sectional profile (B-B'), taken perpendicular to the edge away from the two pile-ups and aligned with a ridge, was used for comparison. In 0-degree indentations (Fig. 9(c,g)), for the A-A' profile, the height of the pile-ups next to the two inclined edges on both sides appeared similar, measuring approximately 73 nm and 130 nm when P_{max} was 20 mN and 50 mN, respectively; for the B-B' profile, the surfaces outside the indent remained flat. In contrast, in 30-degree indentations (Fig. 9(d,h)), for the A-A' profile, the pile-up height at the corner side was measured to be approximately 92 nm and 170 nm when P_{max} was 20 mN and 50 mN, respectively, with the pile-up height at the edge side being even larger. However, for the B-B' profile, the surfaces outside the indent remained flat. This observation suggests that dislocation motion along the [0001] direction was restricted. A detailed discussion of this behavior is presented in Section 3.5.

Fig. 10(a,e) and Fig. 10(b,f) illustrate the topographies of the indented surfaces on the (11−20) plane for the 0-degree and 30-degree indentations, respectively. The pile-ups formed along the [1−100] direction, regardless of the indenter orientation, which aligns with the observations in Fig. 7. For both 0-degree and 30-degree indentations, a cross-sectional profile (A-A') of the indent was extracted along the

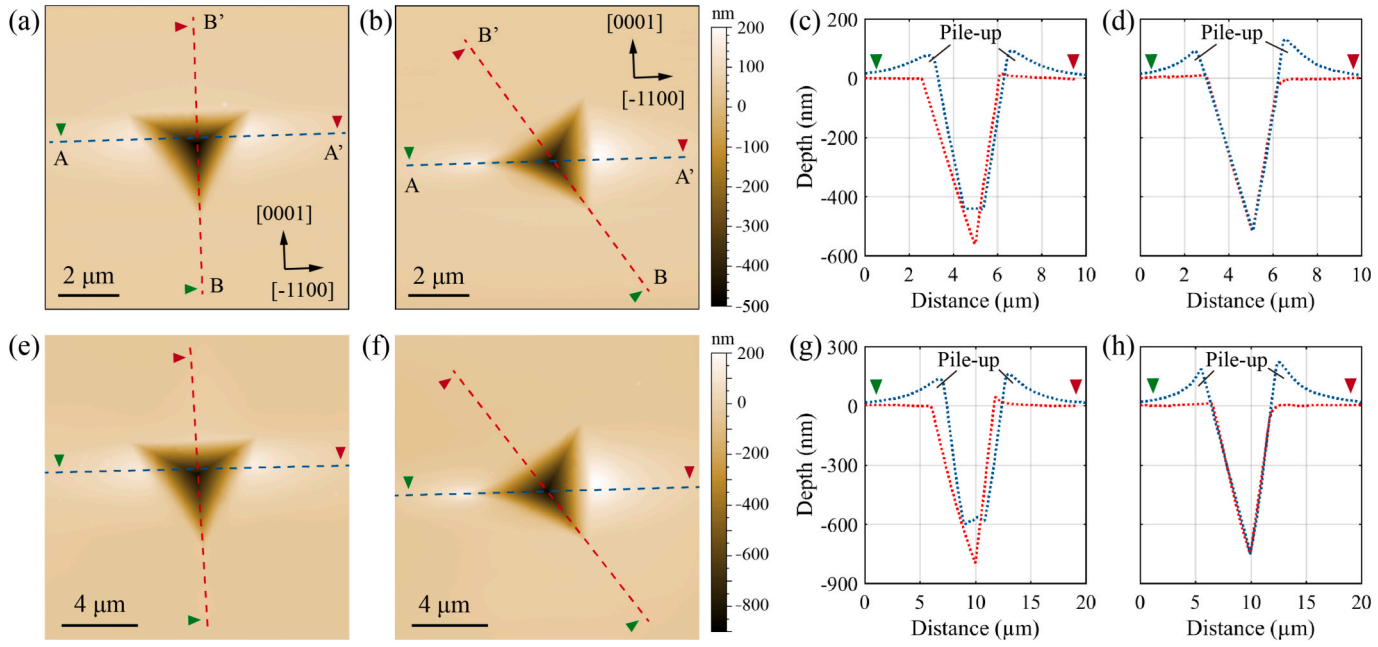

Fig. 10. Topographies of residual indents on the (11−20) plane of ZnO crystals: (a, b) AFM images, and (c, d) cross-sectional profiles of the 0-degree and 30-degree indentations at a maximum load (P_{max}) of 20 mN. Similarly, (e, f) are AFM images, and (g, h) are cross-sectional profiles of the 0-degree and 30-degree indentations at a P_{max} of 50 mN.

[1−100] direction through the two pile-ups, and another cross-sectional profile (B-B') was taken perpendicular to the edge that is away from the two pile-ups. The profiles on the (11−20) plane showed features similar to those on the (1−100) plane: at the same P_{max}, the 30-degree indentation exhibited higher pile-ups but a smaller residual depth compared to the 0-degree indentation.

3.4. Surface structural defects

To evaluate the surface structural defects induced by nanoindentation on each crystal plane, the residual indents were analyzed using panchromatic CL imaging, which captures an averaged CL signal over all detectable wavelengths. This is based on the theory that dislocations act as non-radiative recombination centers, which locally quench the luminescence [39]. Therefore, regions of dark contrast in the CL images correspond to areas with dislocations [40]. Fig. 11 illustrates the CL images of 0-degree and 30-degree indentations on various crystal planes at a P_{max} of 20 mN. The corresponding SEM images captured at the same magnification and location are also presented for comparison.

On the (0001) plane, as shown in Fig. 11(a,b), a continuous dark area appeared around the indents produced by the 0-degree and 30-degree oriented indenters, indicating the formation of high-density dislocations within the residual indents and their vicinity. Furthermore, in the region farther from the indents, the continuous dark area transformed into well-aligned dark spots that extended radially from the center of the residual indents along the <11−20> directions, independent of the indenter orientation, forming a pattern resembling a six-bladed windmill with equal 60° intervals, reflecting the hexagonal symmetry of the (0001) plane. Compared with their corresponding SEM images, it is clear that dislocations propagate over extremely large distances, several times the size of the indents. Similar CL patterns on the ZnO (0001) plane were also observed in indentation tests with a spherical indenter [10] and Vickers indenter [41]. It is noteworthy that the CL pattern caused by indenter contact on ZnO is very different from that on GaN, despite both materials sharing the same crystal structure. In contrast, the dark area in the CL images of the GaN (0001) plane is confined to the vicinity of the residual indents [42]. The above implies that, under nanoindentation, dislocation glide on the ZnO (0001) plane occurs preferentially along the <11−20> directions, independent of the indenter orientation, and that ZnO undergoes more extensive defect formation and plastic deformation than the GaN (0001) plane.

On the (1−100) and (11−20) planes, as shown in Fig. 11(c,d) and Fig. 11(e,f), the CL images of the indents exhibit similar features: under both 0-degree and 30-degree indentations, the dark areas, i.e., the quenching of luminescence, were mainly confined within the indents. Outside the indents, low-contrast dark areas were observed on the left and right sides; however, they did not extend as far as those on the (0001) plane. Furthermore, no dark areas were observed on the upper and lower sides. These observations suggest that, on the (1−100) and (11−20) planes, dislocations induced by indentation tend to propagate in the depth direction rather than parallel to the surface. This point will be further discussed in Section 3.5.

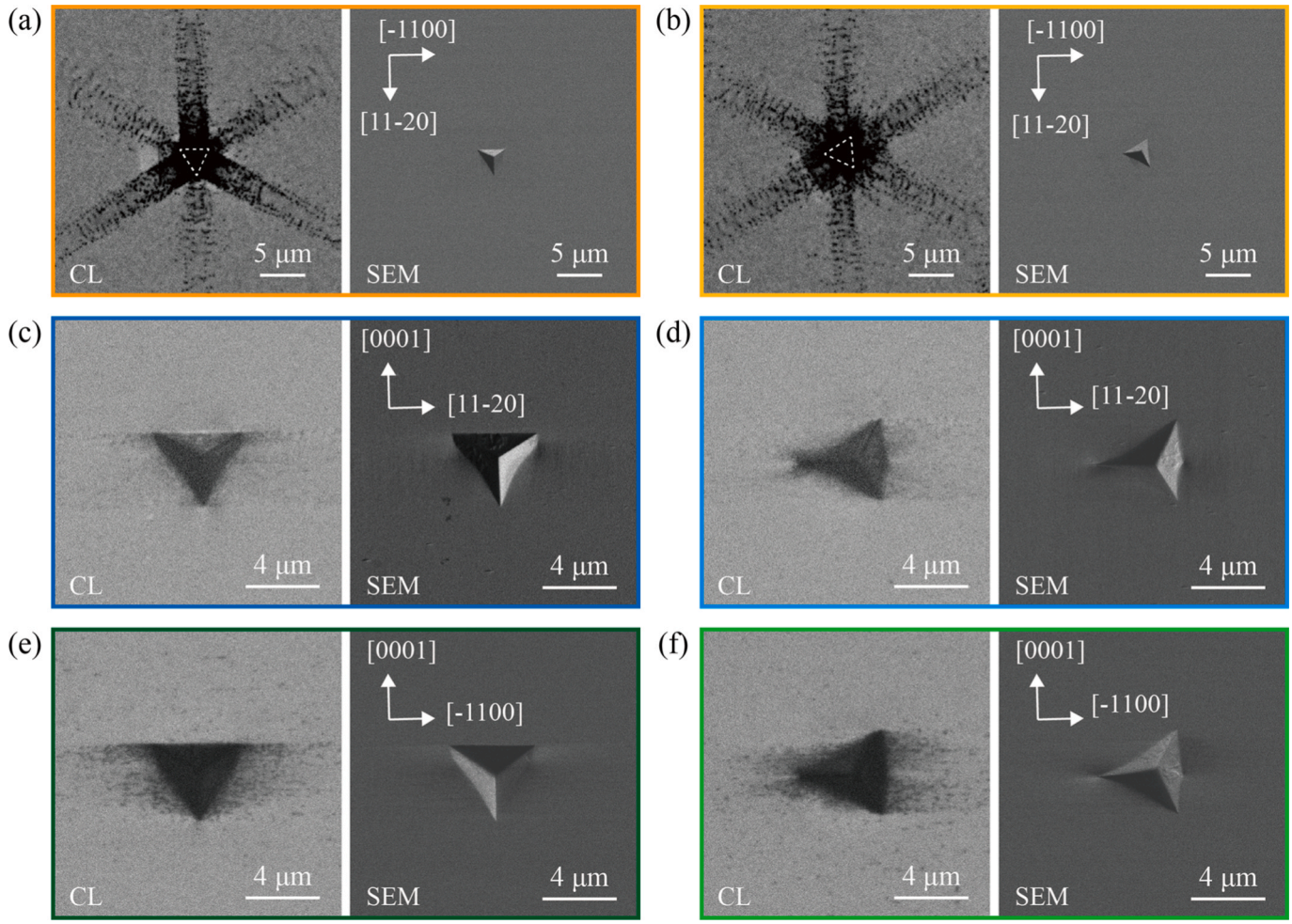

Fig. 11. SEM-Cathodoluminescence (CL) analysis of residual indents at a maximum load of 20 mN on ZnO crystals. (a, b) show 0-degree and 30-degree indentations on the (0001) plane, the dashed white lines outline the edges of the residual indents. Similarly, (c, d) and (e, f) show indentations on the (1−100) and (11−20) plane, respectively.

The surface structural defects were also analyzed using micro-laser Raman microscopy. Since Raman-active phonon modes exhibit orientation- and polarization-dependent intensities [43], the Raman spectra for the pristine surfaces of each crystal plane were first acquired as a reference and plotted as spectrum (i) in Fig. 12. The (0001) plane exhibits two prominent peaks at wavenumbers of 100 and 438 cm^{-1}, corresponding to the low-frequency (E_2^{Low}) and high-frequency (E_2^{High}) nonpolarized modes, respectively, along with a small peak at a wavenumber of 333 cm^{-1}, corresponding to the $E_2^{High}-E_2^{Low}$ phonon difference mode [44]. A small broad band with two indistinct peaks at wavenumbers of 1000 and 1520 cm^{-1} is attributed to second-order scattering $2(E_2^{High} + E_2^{Low})$ combination and non-polar longitudinal optical ($2A_1(LO)$) modes [43], as plotted in Fig. 12(a). In contrast, the (1−100) plane shows that the intensity of the E_2^{Low} and E_2^{High} peaks is greatly suppressed, as plotted in Fig. 12(b). A distinct peak appears at 378 cm^{-1}, corresponding to the transverse-optical (TO) phonon mode with A_1 symmetry, in which phonons are polarized along the *c*-axis of the ZnO crystal. Additionally, a small peak appears between the A_1(TO) and E_2^{High} peaks, corresponding to the TO phonon mode with E_1 symmetry, in which the phonons are polarized perpendicular to the *c*-axis of the ZnO crystal [44]. The (11−20) plane shows a spectrum similar to that of the (0001) plane, except for an additional distinct A_1(TO) peak and a small E_1(TO) peak, as plotted in Fig. 12(c).

The Raman spectra for the surfaces indented under various indenter orientations and maximum loads were then acquired and plotted as spectra (ii-v) in Fig. 12. It is clear that on each crystal plane, the spectra of indented surfaces exhibit identical features to the spectrum of the pristine surface, indicating that nanoindentation did not cause a phase transformation in ZnO crystals, nor did it significantly reduce their crystallinity. This is different from the nanoindentation of GaN crystals, which could led to the appearance of a new Raman peak [45] or significant broadening of the main Raman peak [46]. However, when examining the wavenumber shift of the highest-intensity peak for each plane, as shown in the insets of Fig. 12, the peaks of the indented surfaces shift slightly to higher wavenumbers compared to the pristine surface, with a larger P_{max} resulting in a more pronounced shift and a corresponding decrease in peak intensity. This suggests that compressive residual stresses are generated in the indented surfaces, and lattice distortion occurs due to nanoindentation. It has been reported that bulk ZnO undergoes a phase transformation to the rock-salt structure at a hydrostatic pressure of ~ 9 GPa using a membrane diamond anvil cell [47]. However, in the nanoindentation tests conducted in this study, no such phase transformation was observed on any of the three crystal planes. This is likely because the stress field generated by nanoindentation is dominated by non-hydrostatic pressure.

3.5. Subsurface structural characteristics

The surface morphology and topography of residual indents and the nanoindentation-induced surface defects have been confirmed to be distinct on different crystal planes. Therefore, the subsurface structural characteristics on each crystal plane were characterized to enhance the understanding of the underlying mechanisms.

3.5.1. (0001) plane of ZnO

On the (0001) plane, the cross-sectional TEM image of the residual indent formed by 0-degree indentation is shown in Fig. 13(a), which was taken along the [−1100] zone axis, as evidenced by the selected area diffraction (SAED) pattern in the inset. Mechanical contact by the indenter led to clear observations of two long, straight slip traces parallel to the workpiece surface at distances of 0.82 μm and 1.2 μm beneath the indented surface, labeled as I and II. Additionally, a large number of dislocations were observed in the subsurface, with a particularly high density above slip trace I, as shown in Fig. 13(b). The dislocation density in the area between slip traces I and II decreased, with some dislocation lines identified, which form angles of 60° relative to the slip traces, as shown in Fig. 13(c). These dislocations are supposed to occur on the (10−11) plane because the intersection line of this plane with the (−1100) plane formed a 60° angle with the [11−20] direction. However, below slip trace II, dislocations abruptly disappeared. The Burgers vectors $\boldsymbol{b}$ of the dislocations were investigated under two-beam conditions using three diffraction vectors, namely $\boldsymbol{g}$ = 11−20, $\boldsymbol{g}$ = 11−2−2, and $\boldsymbol{g}$ = 0002, as shown in Fig. 13(d-f), respectively. The horizontal dislocations, which formed on the (0001) plane, were clearly observed under $\boldsymbol{g}$ = 11−20, while they became invisible under the $\boldsymbol{g}$ = 0002 diffraction condition. This indicates that these dislocations correspond to <*a*> dislocations with $\boldsymbol{b}$ = 1/3 <11−20>, according to the $\boldsymbol{g}.\boldsymbol{b}$ criterion (Table S1). In contrast, the inclined dislocations that formed on the (10−11) plane were observable under all three diffraction conditions, indicating that these dislocations correspond to <*c* + *a*> dislocations with $\boldsymbol{b}$ = 1/3 <11−23>.

Fig. 13(g) shows an overview of the cross-sectional TEM image of the residual indent from a 30-degree indentation, taken along the [11−20] zone axis. Numerous dislocations formed in the subsurface, but their generation abruptly stopped at the boundary indicated by the yellow dashed line, at a depth approximately equal to the slip trace I shown in Fig. 13(a). Enlarging the area right beneath the indented surface and further below, as shown in Fig. 13(h,i), it is observed that above the

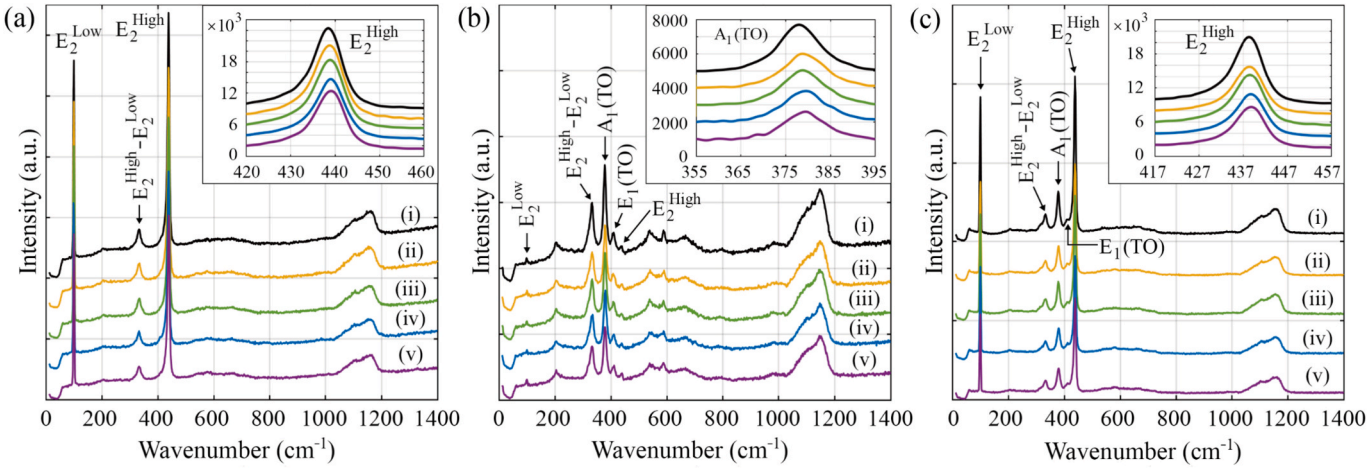

Fig. 12. Raman spectra of ZnO crystals: (a) the (0001) plane, (b) the (1−100) plane, and (c) the (11−20) plane. Spectrum (i) corresponds to the pristine surface, while (ii, iii) represent the indented surfaces with 0-degree and 30-degree oriented indenters at P_{max} = 20 mN. Similarly, (iv, v) correspond to the indented surfaces with 0-degree and 30-degree oriented indenters at P_{max} = 50 mN.

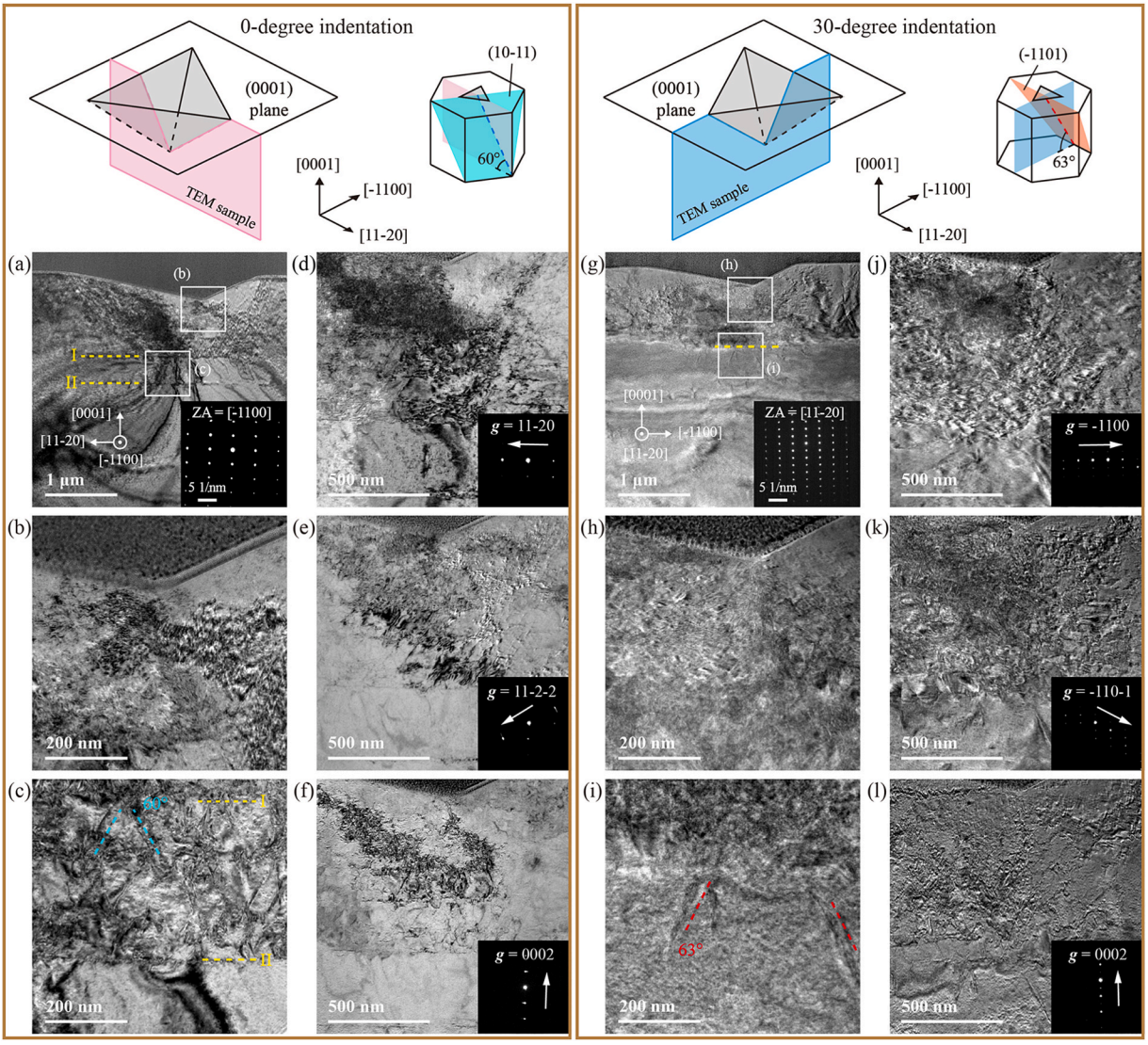

Fig. 13. Cross-sectional TEM observations of the subsurface region beneath the residual indents on the ZnO (0001) plane: (a) overall view of a 0-degree indentation along the zone axis (ZA) of [−1100]; (b, c) close-up views of the regions right beneath and deeper below the indented surface, respectively; (d-f) subsurface images captured under two-beam conditions with different diffraction vectors ***g***. Similarly, (g-i) are subsurface of a 30-degree indentation along the ZA of [11−20]; (j-l) are subsurface images captured under two-beam conditions with different ***g***.

boundary, the dislocation density decreased slightly with increasing depth. Below the boundary, however, the dislocation density decreased dramatically, with only a few dislocation lines being formed. These dislocation lines were oriented at an angle of 63° relative to the [−1100] direction, suggesting that they formed on the (−1101) plane. The images obtained under the two-beam $\boldsymbol{g} = -1100$, $\boldsymbol{g} = -110-1$, and $\boldsymbol{g} = 0002$ diffraction conditions are shown in Fig. 13(j-l). The horizontal dislocations on the (0001) plane were invisible under $\boldsymbol{g} = 0002$, while they were visible under the other diffraction conditions, suggesting that these dislocations correspond to <*a*> dislocations. Additionally, the inclined dislocations on the (−1101) plane were visible under $\boldsymbol{g} = 0002$, suggesting that these dislocations correspond to $<c + a>$ dislocations. These observations indicate that indentation of the ZnO (0001) plane primarily activated the basal slip system (0001) <11−20> and the pyramidal slip system {10−11} <11−23>, which is consistent with the findings reported in [10]. High-resolution TEM images of the subsurface structure (Fig. S9) indicate that no phase transformation occurred, which is consistent with the Raman results.

3.5.2. *(1−100) plane of ZnO*

On the (1−100) plane, the cross-sectional TEM image of the residual indent produced by a 0-degree indentation is shown in Fig. 14(a), taken along the [11−20] zone axis. In contrast to the subsurface of residual indents on the (0001) plane, the dislocation distribution penetrated more than five times deeper, reaching approximately 7 μm in depth beneath the residual indent. However, the dislocation distribution in the lateral direction was confined to the width of the indenter contact, with the maximum dislocation distribution width observed at the contact surface. As the depth increased, the dislocation distribution width gradually narrowed, forming an inverted triangle, as depicted by the dashed yellow line. Upon further magnification, dense dislocations were observed right beneath the indented surface, as shown in Fig. 14(b). The dislocation density then began to decrease with increasing depth, with the dislocations appearing as short lines, measuring tens of nanometers in length, as shown in Fig. 14(c). The same subsurface area in Fig. 14(c) was subsequently analyzed along beam directions [11−20] and [10−10], providing three ***g*** vectors for imaging under two-beam conditions (Table S2). The dislocation lines became invisible under $\boldsymbol{g} = 0002$, as shown in Fig. 14(d), but were observed in both $\boldsymbol{g} = 1-210$ and

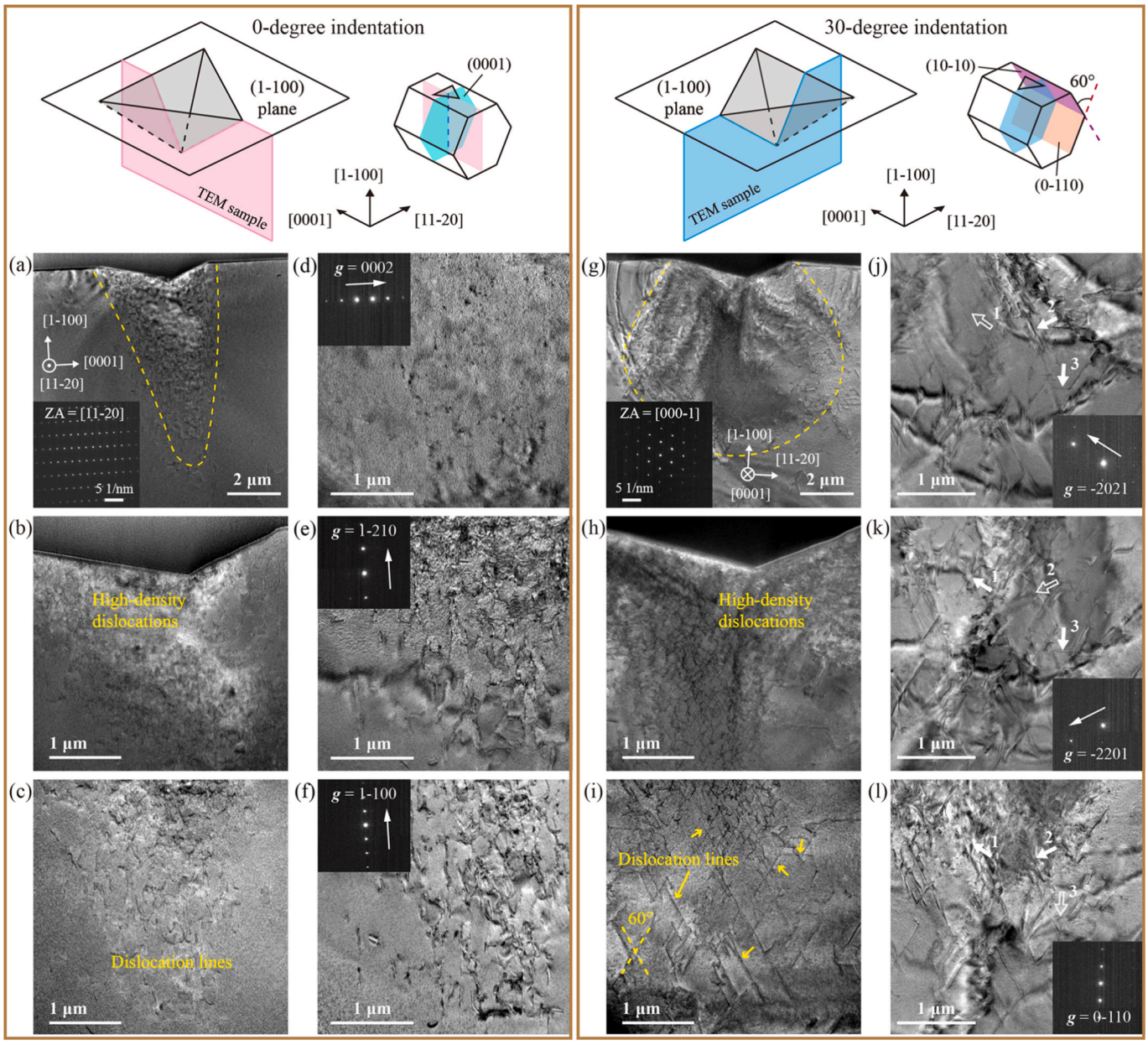

Fig. 14. Cross-sectional TEM observations of the subsurface region beneath the residual indents on the ZnO (1−100) plane: (a) overall view of a 0-degree indentation along the zone axis (ZA) of [11−20]; (b, c) close-up views of the regions right beneath and deeper below the indented surface, respectively; (d-f) the subsurface region in (c) imaged under two-beam conditions with different diffraction vectors ***g***. Similarly, (g-i) are the subsurface of a 30-degree indentation along the ZA of [000−1]; (j-l) are the subsurface region in (i) imaged under two-beam conditions with different ***g***, where white arrows with identical numbers indicate the same dislocation line imaged under different ***g***.

g = 1−100, as shown in Fig. 14(e,f), indicating that the 0-degree indentation-induced dislocations belong to the <*a*> dislocations. Moreover, these dislocation lines are mainly aligned perpendicular to the workpiece surface, indicating their formation on the (0001) plane.

Fig. 14(g) shows an overview of a cross-sectional TEM image of a 30-degree indentation on the (1−100) plane, taken along the [000−1] zone axis. The dislocation distribution width near the surface was close to the indenter contact width, but as the depth increased, it expanded laterally and then narrowed to zero. This resulted in a shape resembling the major arc of a circle, as outlined by the dashed yellow line, while the depth of the dislocation distribution was comparable to that in the 0-degree indentation. At higher magnification, a dense network of dislocations was observed right beneath the indented surface, as shown in Fig. 14(h). The dislocation density decreased with increasing depth, and the dislocations appeared as long, straight lines, each approximately a few hundred nanometers in length, as indicated in Fig. 14(i). Additionally, these dislocations intersected at an angle of 60°, corresponding to the intersection lines of the {01−10} with the (0001) plane. The same subsurface area in Fig. 14(i) was subsequently analyzed along the beam direction [−211−6] and [000−1] for two-beam conditions imaging under ***g*** = −2021, ***g*** = −2201, and ***g*** = 0−110, as shown in Fig. 14(j-l), respectively. The dislocations with three typical directions are marked with numbered arrows, where the same numbers in the figures correspond to the same dislocation line imaged with different ***g***. The dislocation line indicated by arrow 1 exhibited a clear dislocation contrast in Fig. 14(k,l) but not in Fig. 14(j). Similarly, the dislocation line indicated by arrow 2 showed a clear contrast in Fig. 14(j,l) but not in Fig. 14(k). The dislocation line indicated by arrow 3 displayed a clear contrast in Fig. 14(j,k), while it was absent in Fig. 14(l). These observations indicate that the three types of dislocations correspond to ***b*** = 1/3[−12−10], ***b*** =

1/3[11−20], and $\boldsymbol{b}$ = 1/3[−2110], respectively, all of which are <a> dislocations. The above results suggest that the indentation of the ZnO (1−100) plane primarily activated the basal slip system (0001) <11−20> and the {01−10} <11−20> prismatic slip system, which is consistent with the findings reported in [19], except for the absence of the pyramidal slip system in this study. High-resolution TEM images of the subsurface structure and the corresponding strain maps generated by geometric phase analysis (GPA) [48], as shown in Fig. S10, confirm that no phase transformation occurred and that high-density dislocation presented right beneath the residual indents.

3.5.3. (11−20) plane of ZnO

On the (11−20) plane, the cross-sectional TEM image of the residual indent resulting from 0-degree indentation is shown in Fig. 15(a), taken along the [1−100] zone axis. A significant number of dislocations formed in the subsurface region, extending to a depth beneath the residual indent comparable to that observed in the subsurface of the (1−100) plane. The dislocation distribution was widest near the surface, which was approximately equal to the indenter contact width. As the dislocation distribution extended deeper into the material, its width gradually narrows, forming an inverted triangular shape, as indicated by the dashed yellow line. This dislocation distribution had similar characteristics to that observed in a 0-degree indentation on the (1−100) plane, viewed along the [11−20] zone axis (Fig. 14(a)). Higher magnification views of the areas right beneath and further below the indented surface are presented in Fig. 15(b,c). The dislocation density was very high within a depth range of 2 μm beneath the indented surface, while sparse dislocation lines appeared at greater depths. To obtain a clearer view of the dislocation structures, the same subsurface area shown in Fig. 15(c) was analyzed under two-beam conditions, as shown

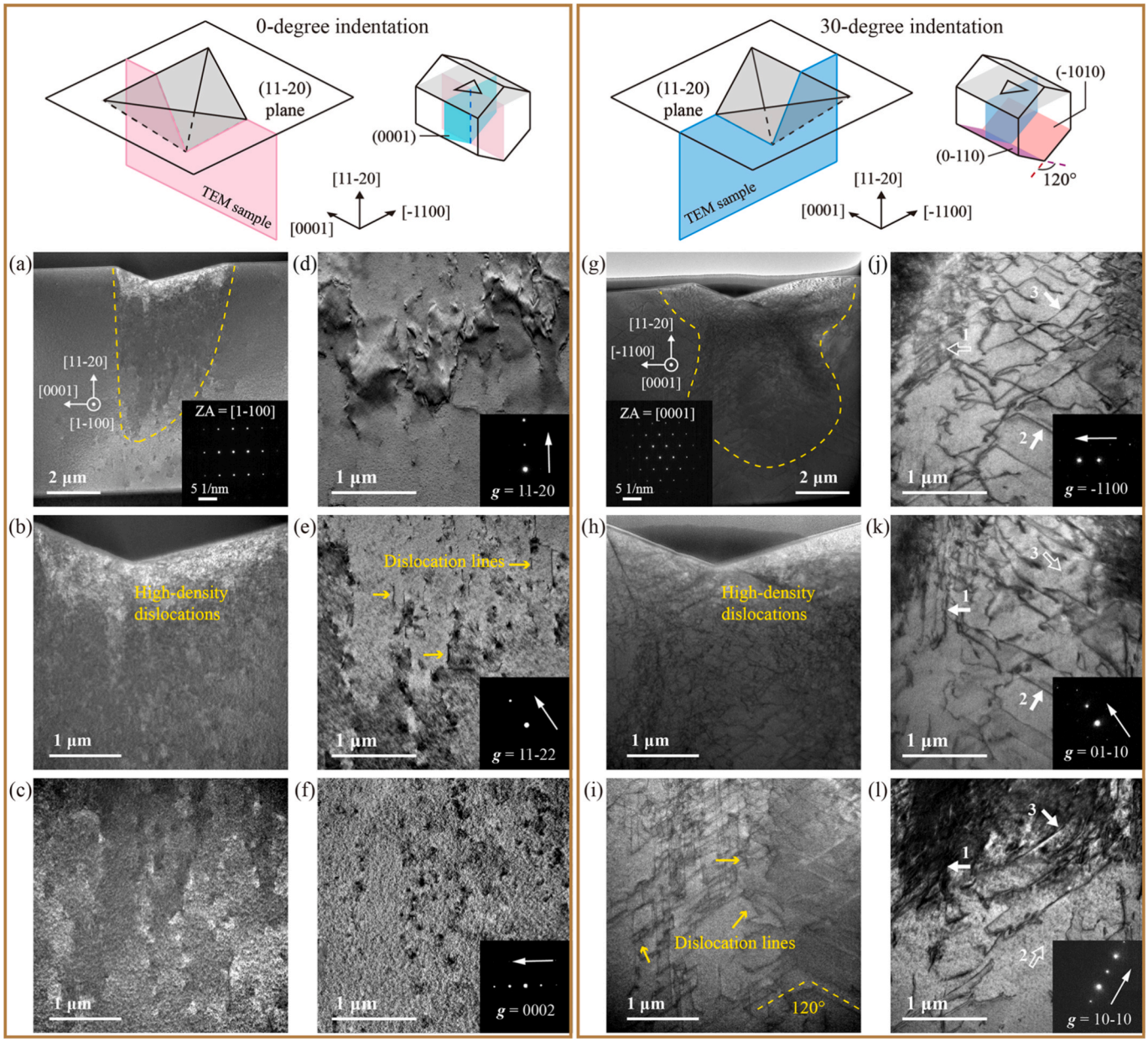

Fig. 15. Cross-sectional TEM observations of the subsurface region beneath the residual indents on the ZnO (11−20) plane: (a) overall view of a 0-degree indentation along the zone axis (ZA) of [1−100]; (b, c) close-up views of the regions right beneath and deeper below the indented surface, respectively; (d-f) the subsurface region in (c) imaged under two-beam conditions with different diffraction vectors $\boldsymbol{g}$. Similarly, (g-i) are the subsurface of a 30-degree indentation along the ZA of [0001]; (j-l) are the subsurface region in (i) imaged under two-beam conditions with different $\boldsymbol{g}$, where white arrows with identical numbers indicate the same dislocation line imaged under different $\boldsymbol{g}$.

in Fig. 15(d-f) and Table S3. The dislocation lines were observed under both $\boldsymbol{g} = 11\bar{2}0$ and $\boldsymbol{g} = 11\bar{2}2$, but became invisible under $\boldsymbol{g} = 0002$, indicating that these dislocations belong to the <a> dislocations. Moreover, most of these dislocation lines were oriented nearly perpendicular to the workpiece surface, suggesting that they were formed on the (0001) plane.

Fig. 15(g) shows an overview of a cross-sectional TEM image of a 30-degree indentation on the $(11\bar{2}0)$ plane, taken along the [0001] zone axis. Compared to the dislocation distribution observed for the 0-degree indentation (Fig. 15(a)), the dislocation distribution width near the surface was greater than the indenter contact width. It then narrowed with increasing depth but expanded at greater depths and eventually narrowed again to zero, forming an hourglass shape, as outlined by the dashed yellow line. Fig. 15(h,i) present higher magnification views of the areas right beneath and deeper below the indented surface. A network of dislocations was observed in the subsurface, with a relatively dense concentration right beneath the indented surface. These dislocations manifested as long, straight lines that were preferentially aligned in the vertical direction or along directions inclined at an angle of 120° (Fig. 15(i)), corresponding to the intersection lines of the $\{1\bar{1}00\}$ planes with the (0001) plane. The same subsurface area in Fig. 15(i) was subsequently analyzed under two-beam conditions $\boldsymbol{g} = \bar{1}100$, $\boldsymbol{g} = 01\bar{1}0$, and $\boldsymbol{g} = 10\bar{1}0$, as shown in Fig. 15(j-l), respectively. The vertical dislocation indicated by arrow 1 exhibited a clear dislocation contrast in Fig. 15(k,l) but not in Fig. 15(j), indicating that this dislocation has $\boldsymbol{b} = 1/3[11\bar{2}0]$ and is classified as an <a> dislocation. The inclined dislocation lines indicated by arrow 2 exhibited a clear contrast in Fig. 15(j,k) but not in Fig. 15(l), while those indicated by arrow 3 were visible in Fig. 15(j,l) but absent in Fig. 15(k). These observations indicate that the dislocations correspond to $\boldsymbol{b} = 1/3[\bar{1}\bar{2}10]$ and $\boldsymbol{b} = 1/3[\bar{2}110]$, respectively, both of which are also classified as <a> dislocations. The above results suggest that the indentation of the ZnO $(11\bar{2}0)$ plane primarily activated the basal slip system (0001) $<11\bar{2}0>$ and the $\{01\bar{1}0\}$ $<11\bar{2}0>$ prismatic slip system, similar to those observed for the ZnO $(1\bar{1}00)$ plane. The activation of the latter slip system was not reported in [19]. High-resolution TEM images of the subsurface structure and the corresponding strain maps (Fig. S11) confirm the absence of phase transformation and the presence of high-density dislocations directly beneath the residual indents.

4. Discussion

Overall, based on the above observations and analysis, indentations on the (0001), $(1\bar{1}00)$, and $(11\bar{2}0)$ planes of the ZnO crystal activate distinct slip systems, leading to variations in surface and subsurface characteristics. However, on the same crystal plane, the activation of the slip system was unaffected by indenter orientation. Therefore, the plastic deformation behavior of the material, including the occurrence of pop-in events, the formation of pile-ups, and luminescence quenching, is little affected by the orientation of the indenter. Fig. 16 summarizes the slip systems activated during indentation on each crystal plane of ZnO. The relationship between indentation crystal planes and dislocation slip parameters is summarized in Table 2.

The load–displacement curves of the indentations on the (0001) plane displayed pop-in events, whereas no such events were observed on the $(1\bar{1}00)$ and $(11\bar{2}0)$ planes, irrespective of the maximum load (Fig. 3). On the other hand, based on surface morphology observations, indentations on the (0001) plane exhibit pop-in events without surface cracks occurring (Fig. 5(a)), whereas indentations on the $(1\bar{1}00)$ and $(11\bar{2}0)$ planes do not exhibit pop-in events, yet surface cracks are initiated (Figs. 6 and 7). Therefore, it can be concluded that pop-in events in ZnO crystals do not result from crack formation. Instead, comparative analysis of the subsurface structural characteristics (Figs. 13–15) suggests that the obstruction of dislocation glide along the depth direction by basal plane slip is responsible for the occurrence of

Table 2
Summary of the relationship between indentation crystal planes and dislocation slip parameters.

Indentation plane	Activated slip planes	Burgers vectors
(0001)	(0001) and $\{10\bar{1}1\}$	<a> and <a + c>
$(1\bar{1}00)$	(0001) and $\{01\bar{1}0\}$	<a>
$(11\bar{2}0)$	(0001) and $\{01\bar{1}0\}$	<a>

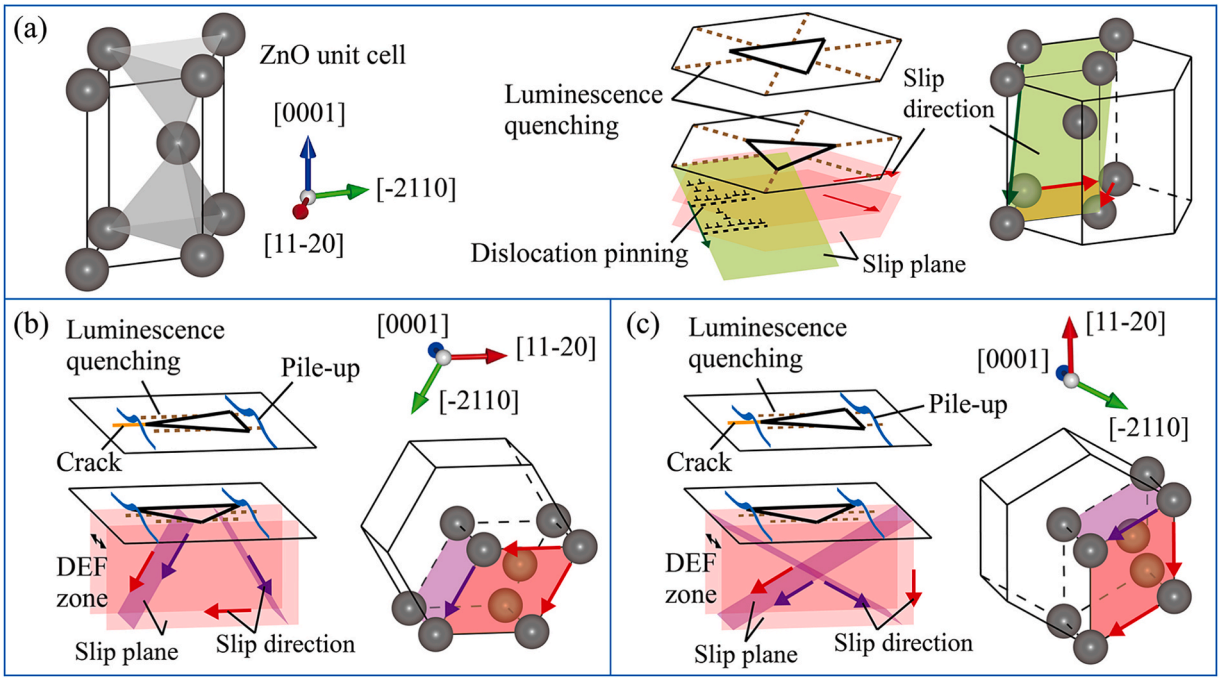

Fig. 16. Schematics of macroscopic deformation and microstructural evolution in ZnO crystals during indentation: on (a) the (0001) plane, (b) the $(1\bar{1}00)$ plane, and (c) the $(11\bar{2}0)$ plane. The deformation zone is abbreviated to DEF zone.

pop-in events. Specifically, for indentations on the (0001) plane, the basal and pyramidal slip systems are activated, as illustrated in Fig. 16 (a). Once slip activates along the basal planes, further loading tends to favor continued slip within these pre-existing slip bands, rather than the activation of new slip systems deeper into the material. As a result, dislocations tend to glide along the basal planes, forming slip bands that extend laterally (Fig. 13(a)). This is also evidenced by the CL images shown in Fig. 11(a,b), where quenching of the luminescence band extends over a long distance along the <11−20> directions. These slip bands can serve as "pinning sites" for dislocations on pyramidal planes, hindering their further propagation [49]. This pinning mechanism prevents smooth deformation, causing stress to build up locally, leading to further pop-in events when the stress exceeds the critical threshold for activating new slip in deeper regions. Additionally, the restriction of dislocation motion may contribute to higher elastic recovery during unloading, as a larger portion of the deformation remains elastic until the onset of plastic slip.

In contrast, for indentations on the (1−100) and (11−20) planes, the basal and prismatic slip systems are activated, as illustrated in Fig. 16(b, c). As the basal plane is parallel to the loading axis, the pinning effect on the basal planes does not act as a barrier to dislocation glide on prismatic planes along the depth direction. Thus, the dislocation distributions in the (1−100) and (11−20) planes (Fig. 14(a) and 15(a)) extend much deeper than that in the (0001) plane (Fig. 13(a)). However, since basal and prismatic slip systems cannot accommodate dislocation glide along the [0001] direction, the deformation (DEF) zone in this direction is confined to the contact width of the indenter for both the (1−100) and (11−20) planes. Consequently, the initiated dislocations not only glide in the depth direction but also tend to glide toward the surface with minimal resistance, facilitating outward material flow and resulting in pronounced pile-up. Specifically, pile-ups occur along the [11−20] direction for indentations on the (1−100) plane and along the [1−100] direction for indentations on the (11−20) plane. The restricted DEF zone in the [0001] direction is also evident in the CL images shown in Fig. 11 (c-f), where luminescence quenching in the [0001] direction is confined to the indenter contact area, and in the cross-sectional TEM images in Fig. 14(a) and 15(a), where the dislocation distribution in the lateral direction is confined to the indenter contact width. In addition, because neither the basal nor prismatic slip systems accommodate dislocation glide in the [0001] direction, the capacity for resistance to crack formation along this direction, i.e., fracture toughness in [0001] direction, is significantly limited. Consequently, under the 30-degree indentation on the (1−100) and (11−20) planes (Fig. 6(e-f) and 7(e-f)), a long crack was initiated at one corner of the indent. This corner was aligned with the indenter ridge that was oriented perpendicular to the [0001] direction, generating the highest tensile stress along this direction.

From a machining perspective, the slip systems activated in the (0001) plane differ from those in the (10–10) and (11–20) planes, and therefore the subsurface damage induced during machining of the (0001) plane is expected to exhibit distinct characteristics compared to those observed in the other two planes. For example, during abrasive machining of the ZnO workpiece, dislocations are nucleated in the subsurface while grit scratches the surface, as schematically illustrated in Fig. S12(a). When the (0001) plane is scratched, dislocations are confined near the subsurface but extend parallel to the surface over a long distance along the <11–20> directions, reaching into areas beyond the scratched region. In contrast, when the (10–10) and (11–20) planes are scratched along the [11–20] and [1–100] directions, respectively, dislocations are confined within the contact width but penetrate more deeply into the subsurface, causing a thicker subsurface damage layer. On the other hand, the fracture anisotropy of the (1−100) and (11−20) planes is relatively more pronounced than that of the (0001) plane. Thus, when scratching the (1−100) and (11−20) planes, cracks may form on the scratched surface, with their extent governed by the scratching direction; the volume of pile-ups forming along the sides of the scratched groove also varies depending on the scratching direction, as schematically illustrated in Fig. S12(b). In addition, when machining the (0001) plane, the turning process, in which the cutting direction continuously changes relative to the crystal orientation, is considered acceptable. However, ploughing should be carefully avoided, as the elastic recovery rate of the (0001) plane is high, which may result in submicron-pits on the machined surface after the tool passes [29]. However, it is also worth noting that crack formation in brittle solids, such as ceramic and semiconductor oxides at room temperature, heavily depends on factors such as testing length scale, loading rate, and crystal orientation. In the specific case of nanoindentation on oxides, the tip radius and the applied maximum load can also play a critical role in addition to the crystal orientation [50]. Therefore, accurately correlating nanoindentation results with actual mechanical processing still requires further investigation.

5. Conclusions

In this study, nanoindentation tests were performed on *c*-plane (0001), *m*-plane (1−100), and *a*-plane (11−20) ZnO crystals using a Berkovich indenter at different indenter orientations. Corresponding load–displacement curves, surface features (morphologies and topographies), as well as surface and subsurface structural defects were systematically analyzed. These characteristics for all three crystal planes were compared. The mechanism of the crystal orientation-dependent surface morphology and topography evolution in ZnO crystals under mechanical loading was elucidated. Main conclusions are summarized as follows.

(1) Indentations on the ZnO (0001) plane activate basal and pyramidal slip systems, while indentations on the ZnO (1−100) and (11−20) planes activate basal and prismatic slip systems. The Burgers vectors of dislocations on the three crystal planes are determined through TEM under two-beam conditions. The activation of these slip systems is independent of the indenter orientation. The mechanical contact-induced subsurface defects tend to be confined near the surface on the (0001) plane, whereas they extend deeper into the subsurface on the (1−100) and (11−20) planes.

(2) On the ZnO (0001) plane, no pile-up formation was detected on the indented surface. Multiple pop-in events in the load–displacement curve occurred randomly during the loading phase, while significant elastic recovery was observed during the unloading phase. These phenomena are attributed to the slip bands along the basal plane, which act as pinning sites for dislocations on the pyramidal planes. On the ZnO (1−100) and (11−20) planes, pile-up formations were formed along the [11−20] and [1−100] directions, respectively, regardless of the indenter orientation. This occurs because the activated basal and prismatic slip systems cannot accommodate dislocation glide along the [0001] direction.

(3) For ZnO crystals, indentation did not induce a phase transformation or a significant reduction in crystallinity, as evidenced by Raman spectroscopy. This contrasts with GaN crystals, where a new peak appeared or broadening of the main peak occurred in the Raman spectrum of their indented surfaces. The ZnO (0001) plane undergoes more extensive defect formation and plastic deformation than the GaN (0001) plane, as the luminescence quenching band caused by dislocations under indentation extends significantly farther in ZnO than in GaN. The luminescence quenching bands on the ZnO (1−100) and (11−20) planes are restricted along these planes because dislocations tend to propagate perpendicular to these planes, extending in depth.

(4) On the ZnO (0001) plane, the critical load for generating cracks is much lower than that required on the GaN (0001) plane. Ridge and edge cracks are initiated during the loading and unloading phases, respectively. The extent of cracking is more pronounced

when the indenter ridge is oriented along the [1−100] direction than along the [11−20] direction. On the ZnO (1−100) and (11−20) planes, a long corner crack tends to occur during the loading phase when the indenter ridge is oriented along the [0001] direction. The (1−100) and (11−20) planes exhibit stronger fracture anisotropy than the (0001) plane. However, lattice rotation and subgrain formation tend to occur in the (0001) plane rather than in the (1−100) and (11−20) planes.

The study provides a comprehensive understanding of the evolution of crystal orientation-dependent surface morphology and topography in ZnO crystals under mechanical loading, which has been overlooked in previous studies. The findings provide insights into the development of advanced machining techniques and the optimization of processing parameters to enhance the manufacturing of ZnO components with different crystal orientations.

CRediT authorship contribution statement

Weihai Huang: Writing – original draft, Visualization, Methodology, Investigation, Formal analysis, Data curation, Conceptualization. **Jiwang Yan:** Writing – review & editing, Visualization, Supervision, Methodology, Funding acquisition, Conceptualization.

Declaration of competing interest

The authors declare that they have no known competing financial interests or personal relationships that could have appeared to influence the work reported in this paper.

Acknowledgement

This work has been partially supported by Japan Society for the Promotion of Science under the Grant-in-Aid for JSPS Fellows, project number 24KF0255, and the Grant-in-Aid for Scientific Research (A), project number 25H00709.

Appendix A. Supplementary data

Supplementary data to this article can be found online at https://doi.org/10.1016/j.matdes.2025.114531.

Data availability

Data will be made available on request.

References

[1] D. Debnath, D. Sen, T.T. Neog, B. Saha, S.K. Ghosh, Growth of ZnO polytypes: multiple facets of diverse applications, Cryst. Growth Des. 24 (3) (2024) 871–885.
[2] Z. Dong, X. Zhang, S. Peng, F. Jin, Q. Wan, J. Xue, X. Yi, Mechanical properties of GaN single crystals upon C ion irradiation: nanoindentation analysis, Materials 15 (2022).
[3] D.A. Lucca, M.J. Klopfstein, R. Ghisleni, G. Cantwell, Investigation of polished single crystal ZnO by nanoindentation, CIRP Ann. 51 (1) (2002) 483–486.
[4] E. Darnbrough, J. Aspinall, M. Pasta, D.E.J. Armstrong, Elastic and plastic mechanical properties of lithium measured by nanoindentation, Mater. Des. 233 (2023) 112200.
[5] M. Seehaus, S. Lee, T. Stollenwerk, J.M. Wheeler, S. Korte-Kerzel, Estimation of directional single crystal elastic properties from nano-indentation by correlation with EBSD and first-principle calculations, Mater. Des. 234 (2023) 112296.
[6] S. Bruns, L. Petho, C. Minnert, J. Michler, K. Durst, Fracture toughness determination of fused silica by cube corner indentation cracking and pillar splitting, Mater. Des. 186 (2020) 108311.
[7] G. Han, B. Lee, S. Lee, C. Jeong, H. Lee, Evaluation of plastic properties and equi-biaxial residual stress via indentation and ANN, Mater. Des. 239 (2024) 112745.
[8] A. Sciuto, P.P. Barbarino, D. Mello, G. D'Arrigo, Insight on defects mechanically introduced by nanoindentation in 4H-SiC p-n diode, Mater. Des. 239 (2024) 112751.
[9] S.O. Kucheyev, J.E. Bradby, J.S. Williams, C. Jagadish, M.V. Swain, Mechanical deformation of single-crystal ZnO, Appl. Phys. Lett. 80 (6) (2002) 956–958.
[10] J.E. Bradby, S.O. Kucheyev, J.S. Williams, C. Jagadish, M.V. Swain, P. Munroe, M. R. Phillips, Contact-induced defect propagation in ZnO, Appl. Phys. Lett. 80 (24) (2002) 4537–4539.
[11] X. Zhu, J. Li, L. Zhang, F. Lang, X. Hou, X. Zhao, W. Zhang, C. Zhao, Z. Yang, Effect of strain rate on nano-scale mechanical behavior of a-plane (11−20) ZnO single crystal by nanoindentation, Micromachines 14 (2) (2023) 404.
[12] Y. Kim, I. Choi, J. Lee, M. Seok, J. Jang, Strain-dependent transition of time-dependent deformation mechanism in single-crystal ZnO evaluated by spherical nanoindentation, Phil. Mag. 95 (16–18) (2015) 1896–1906.
[13] C. Gao, G. Liu, R. Yang, O. Zakharov, Y. Geng, C. Li, Understanding crack initiation and propagation mechanisms of ZnO crystals induced by nanoindentation and nanoscratch, Mater. Today Commun. 45 (2025) 112425.
[14] S. Basu, M.W. Barsoum, Deformation micromechanisms of ZnO single crystals as determined from spherical nanoindentation stress–strain curves, J. Mater. Res. 22 (9) (2007) 2470–2477.
[15] T.H. Sung, J.C. Huang, H.C. Chen, Mechanical response of polar/non-polar ZnO under low dimensional stress, Appl. Phys. Lett. 102 (24) (2013) 241901.
[16] R.M. Juday, E.Y. Silva, J.G. Huang, P. Caldas, R. Prioli, F.A. Ponce, Strain-related optical properties of ZnO crystals due to nanoindentation on various surface orientations, J. Appl. Phys. 113 (18) (2013) 183511.
[17] P.H. Lin, X.H. Du, Y.H. Chen, H.C. Chen, J.C. Huang, Nano-scaled diffusional or dislocation creep analysis of single-crystal ZnO, AIP Adv. 6 (9) (2016) 095125.
[18] Y. Li, X. Fang, E. Tochigi, Y. Oshima, S. Hoshino, T. Tanaka, H. Oguri, S. Ogata, Y. Ikuhara, K. Matsunaga, A. Nakamura, Shedding new light on the dislocation-mediated plasticity in wurtzite ZnO single crystals by photoindentation, J. Mater. Sci. Technol. 156 (2023) 206–216.
[19] H. Oguri, Y. Li, X. Fang, A. Nakamura, Photoplastic anisotropy in nanoindentation of wurtzite ZnO single crystals, Appl. Phys. Lett. 126 (11) (2025) 114101.
[20] W. Huang, J. Yan, Towards understanding the mechanism of vibration-assisted cutting of monocrystalline silicon by cyclic nanoindentation, J. Mater. Process. Technol. 311 (2023) 117797.
[21] D. Axinte, H. Huang, J. Yan, Z. Liao, What micro-mechanical testing can reveal about machining processes, Int. J. Mach. Tool Manu. 183 (2022) 103964.
[22] H.A. Kishawy, M.A. Elbestawi, Effects of process parameters on material side flow during hard turning, Int. J. Mach. Tool Manu. 39 (7) (1999) 1017–1030.
[23] J. Yan, Laser micro-Raman spectroscopy of single-point diamond machined silicon substrates, J. Appl. Phys. 95 (4) (2004) 2094–2101.
[24] M. Matsumoto, H. Huang, H. Harada, K. Kakimoto, J. Yan, On the phase transformation of single-crystal 4H-SiC during nanoindentation, J. Phys. D Appl. Phys. 50 (26) (2017) 265303.
[25] W. Huang, J. Yan, Mechanisms of tool-workpiece interaction in ultraprecision diamond turning of single-crystal SiC for curved microstructures, Int. J. Mach. Tool Manu. 191 (2023) 104063.
[26] Z. Zhang, Q. Yan, Y. Zhang, H. Wang, Z. Tong, X. Jiang, New insights into the deformation mechanism of orientation-dependent nanoindentation behaviours, Tribol. Int. 200 (2024) 110112.
[27] S. Goel, N. Haque Faisal, X. Luo, J. Yan, A. Agrawal, Nanoindentation of polysilicon and single crystal silicon: Molecular dynamics simulation and experimental validation, J. Phys. D Appl. Phys. 47 (27) (2014) 275304.
[28] J. Chen, F. Ding, X. Luo, X. Rao, J. Sun, Fundamental study of ductile-regime diamond turning of single crystal gallium arsenide, Precis. Eng. 62 (2020) 71–82.
[29] W. Huang, J. Yan, Surface formation mechanism in ultraprecision diamond turning of coarse-grained polycrystalline ZnSe, Int. J. Mach. Tool Manu. 153 (2020) 103554.
[30] U. Diebold, L.V. Koplitz, O. Dulub, Atomic-scale properties of low-index ZnO surfaces, Appl. Surf. Sci. 237 (1) (2004) 336–342.
[31] S. Jian, Mechanical Deformation Induced in Si and GaN under Berkovich Nanoindentation, Nanoscale Res. Lett. 3 (1) (2007) 6.
[32] D.J. Morris, S.B. Myers, R.F. Cook, Sharp probes of varying acuity: Instrumented indentation and fracture behavior, J. Mater. Res. 19 (1) (2004) 16.
[33] M. Cui, H. Huang, C. Wang, Y. Qian, L. Zhang, Z. Zhang, J. Yan, Visualization of indentation induced sub-surface shear bands of Zr-based metallic glass by nanosecond pulse laser irradiation, Vacuum 202 (2022) 111141.
[34] E. Renner, Y. Gaillard, F. Richard, F. Amiot, P. Delobelle, Sensitivity of the residual topography to single crystal plasticity parameters in Berkovich nanoindentation on FCC nickel, Int. J. Plast 77 (2016) 118–140.
[35] R.F. Cook, G.M. Pharr, Direct observation and analysis of indentation cracking in glasses and ceramics, J. Am. Ceram. Soc. 73 (4) (1990) 787–817.
[36] Y. Cheng, C. Cheng, Effects of 'sinking in' and 'piling up' on estimating the contact area under load in indentation, Philos. Mag. Lett. 78 (2) (1998) 115–120.
[37] Y. Wang, D. Raabe, C. Klüber, F. Roters, Orientation dependence of nanoindentation pile-up patterns and of nanoindentation microtextures in copper single crystals, Acta Mater. 52 (8) (2004) 2229–2238.
[38] W.M. Huang, J.F. Su, M.H. Hong, B. Yang, Pile-up and sink-in in micro-indentation of a NiTi shape-memory alloy, Scr. Mater. 53 (9) (2005) 1055–1057.
[39] T. Sugahara, H. Sato, M. Hao, Y. Naoi, S. Kurai, S. Tottori, K. Yamashita, K. Nishino, L.T. Romano, S. Sakai, Direct evidence that dislocations are non-radiative recombination centers in GaN, Jpn. J. Appl. Phys. 37 (4A) (1998) L398.
[40] J. Schreiber, S. Vasnyov, The dynamic mode of high-resolution cathodoluminescence microscopy, J. Phys. Condens. Matter 16 (2) (2004) S75.
[41] Z. Takkouk, N. Brihi, K. Guergouri, Y. Marfaing, Cathodoluminescence study of plastically deformed bulk ZnO single crystal, Phys. B Condens. Matter 366 (1) (2005) 185–191.
[42] S. Jian, Berkovich indentation-induced deformation behaviors of GaN thin films observed using cathodoluminescence and cross-sectional transmission electron microscopy, Appl. Surf. Sci. 254 (21) (2008) 6749–6753.

[43] J. Thyr, L. Österlund, T. Edvinsson, Polarized and non-polarized Raman spectroscopy of ZnO crystals: Method for determination of crystal growth and crystal plane orientation for nanomaterials, J. Raman Spectrosc. 52 (8) (2021) 1395–1405.
[44] B. Cheng, W. Sun, J. Jiao, B. Tian, Y. Xiao, S. Lei, Disorder-induced Raman scattering effects in one-dimensional ZnO nanostructures by incorporation and anisotropic distribution of Dy and Li codopants, J. Raman Spectrosc. 41 (10) (2010) 1221–1226.
[45] J. Huang, K. Xu, Y.M. Fan, J.F. Wang, J.C. Zhang, G.Q. Ren, Dislocation luminescence in GaN single crystals under nanoindentation, Nanoscale Res. Lett. 9 (1) (2014) 649.
[46] P. Puech, F. Demangeot, J. Frandon, C. Pinquier, M. Kuball, V. Domnich, Y. Gogotsi, GaN nanoindentation: a micro-Raman spectroscopy study of local strain fields, J. Appl. Phys. 96 (5) (2004) 2853–2856.
[47] F. Decremps, J. Pellicer-Porres, A.M. Saitta, J. Chervin, A. Polian, High-pressure Raman spectroscopy study of wurtzite ZnO, Phys. Rev. B 65 (9) (2002) 092101.
[48] J. Li, W. Zhang, X. Zhao, F. Lang, Y. Xing, Experimental and mechanistic investigation of the residual stress in SiCP/Al composites at the multi scale, Mater. Des. 253 (2025) 113888.
[49] S. Jian, Pop-in effects and dislocation nucleation of c-plane single-crystal ZnO by Berkovich nanoindentation, J. Alloy. Compd. 644 (2015) 54–58.
[50] X. Fang, H. Bishara, K. Ding, H. Tsybenko, L. Porz, M. Höfling, E. Bruder, Y. Li, G. Dehm, K. Durst, Nanoindentation pop-in in oxides at room temperature: Dislocation activation or crack formation? J. Am. Ceram. Soc. 104 (9) (2021) 4728–4741.